

AD-A104 821

WASHINGTON UNIV SEATTLE  
BIOLOGICAL DAMAGE THRESHOLD INDUCED BY ULTRASHORT FUNDAMENTAL, ETC(U)  
DEC 80 A P BRUCKNER, J M SCHURR, E L CHANG F33615-78-C-0616

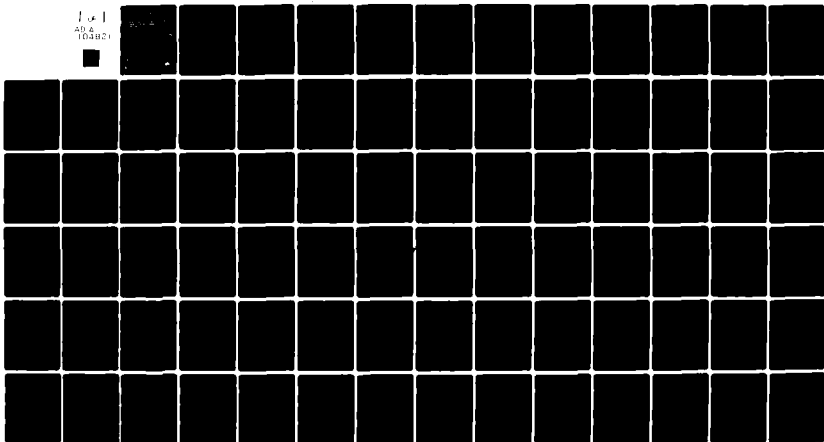
F/6 6/18

NL

UNCLASSIFIED 61-5269

SAM-TR-80-47

104821  
AP 80  
104821



END  
DATE FILMED  
10-81  
DTIC

*Sc*  
Report SAM-TR-80-47

LEVEL

(P)

ADA104821

# BIOLOGICAL DAMAGE THRESHOLD INDUCED BY ULTRASHORT FUNDAMENTAL, 2ND, AND 4TH HARMONIC LIGHT PULSES FROM A MODE-LOCKED Nd:GLASS LASER

Adam P. Bruckner, Ph.D.  
J. Michael Schurr, Ph.D.  
Eddie L. Chang, Ph.D.  
Aerospace and Energetics Research Program  
University of Washington  
Seattle, Washington 98195



December 1980

Final Report for Period April 1978 - January 1980

Approved for public release; distribution unlimited.

DMC FILE COPY

Prepared for  
USAF SCHOOL OF AEROSPACE MEDICINE  
Aerospace Medical Division (AFSC)  
Brooks Air Force Base, Texas 78235



81 9 29 007

## NOTICES

This final report was submitted by Aerospace and Energetics Research Program, University of Washington, Seattle, Washington, under contract F33615-78-C-0616, job order 7757-02-55, with the USAF School of Aerospace Medicine, Aerospace Medical Division, AFSC, Brooks Air Force Base, Texas. Dr. Taboada (USAFSAM/RZL) was the Laboratory Project Scientist-in-Charge.

When U.S. Government drawings, specifications, or other data are used for any purpose other than a definitely related Government procurement operation, the Government thereby incurs no responsibility nor any obligation whatsoever; and the fact that the Government may have formulated, furnished, or in any way supplied the said drawings, specifications, or other data is not to be regarded by implication or otherwise, as in any manner licensing the holder or any other person or corporation, or conveying any rights or permission to manufacture, use, or sell any patented invention that may in any way be related thereto.

The animals involved in this study were procured, maintained, and used in accordance with the Animal Welfare Act of 1970 and the "Guide for the Care and Use of Laboratory Animals" prepared by the Institute of Laboratory Animal Resources - National Research Council.

This report has been reviewed by the Office of Public Affairs (PA) and is releasable to the National Technical Information Service (NTIS). At NTIS, it will be available to the general public, including foreign nations.

This technical report has been reviewed and is approved for publication.

*John Taboada*  
JOHN TABOADA, Ph.D.  
Project Scientist

*John E. Pickering*  
JOHN E. PICKERING, M.S.  
Chief, Radiation Sciences Division

*Roy L. DeHart*  
ROY L. DEHART  
Colonel, USAF, MC  
Commander

## UNCLASSIFIED

SECURITY CLASSIFICATION OF THIS PAGE When Data Entered

REPORT DOCUMENTATION PAGE		READ INSTRUCTIONS BEFORE COMPLETING FORM
1. REPORT NUMBER	12. GOVT ACCESSION NO.	3. RECIPIENT'S CATALOG NUMBER
SAMTR-80-47	AD-A104 821	
4. TITLE (and Subtitle) <b>BIOLOGICAL DAMAGE THRESHOLD INDUCED BY ULTRASHORT FUNDAMENTAL, 2ND, AND 4TH HARMONIC LIGHT PULSES FROM A MODE-LOCKED Nd:GLASS LASER.</b>		5. TYPE OF REPORT & PERIOD COVERED <b>Final Report April 1978 - January 1980.</b>
7. AUTHOR(S) Adam P. Bryckner, Ph.D. J. Michael Schurr, Ph.D. Eddie L. Chang, Ph.D.		6. PERFORMING ORG REPORT NUMBER 61-5269
9. PERFORMING ORGANIZATION NAME AND ADDRESS Aerospace and Energetics Research Program University of Washington Seattle, Washington 98195		10. PROGRAM ELEMENT PROJECT TASK AREA & WORK UNIT NUMBERS 62202F 17 7757402-55
11. CONTROLLING OFFICE NAME AND ADDRESS USAF School of Aerospace Medicine (RZL) Aerospace Medical Division (AFSC) Brooks Air Force Base, Texas 78235		12. REPORT DATE December 1980
14. MONITORING AGENCY NAME & ADDRESS (if different from Controlling Office)		13. NUMBER OF PAGES 82
		15. SECURITY CLASS. (of this report) <b>Unclassified</b>
		15a. DECLASSIFICATION DOWNGRADING SCHEDULE
16. DISTRIBUTION STATEMENT (of this Report) <b>Approved for public release; distribution unlimited.</b>		
17. DISTRIBUTION STATEMENT (of the abstract entered in Block 20, if different from Report)		
18. SUPPLEMENTARY NOTES		
19. KEY WORDS (Continue on reverse side if necessary and identify by block number) Picosecond biological damage Nd:Glass laser, mode-locked Biological macromolecules/DNA, bilipid layer vesicles Laser-induced retinal damage, 530 nm Macaca fascicularis monkey		
20. ABSTRACT (Continue on reverse side if necessary and identify by block number) Selected biological macromolecules and 20 Macaca fascicularis monkey eyes were irradiated with ultrashort pulses of light of various wavelengths derived from a mode-locked Nd:Glass laser in order to determine threshold damage mechanisms. Macromolecules such as calf-thymus DNA, dipalmitoyl phosphatidyl choline vesicles, and egg-yolk lecithin vesicles, which are similar to the constituents of living cells that may be susceptible to damage, were irradiated with single picosecond pulses and entire mode-locked pulse trains of 1060-nm and 530-nm		

## UNCLASSIFIED

SECURITY CLASSIFICATION OF THIS PAGE (When Data Entered)

## 20. ABSTRACT (Continued)

light. DNA was not damaged at any energy density available including levels sufficient to cause dielectric breakdown in water. Experimental studies of electromagnetic stress-induced birefringence in DNA base-pairs were also carried out in an attempt to establish a lower limit on the restraining forces governing tilting of the DNA bases with respect to the helix axis. The irradiation experiments at 1060 nm with the bilipid layer vesicles indicated a damage threshold of  $\sim 600 \text{ mJ/cm}^2$  for entire pulse trains of  $\sim 100$  pulses and  $\sim 9 \text{ mJ/cm}^2$  for single pulses, as determined by dynamic light scattering. In both the multiple- and single-pulse cases, the peak optical electric field incident on the vesicles was  $6-7 \times 10^5 \text{ V/cm}$ , about an order of magnitude above the membrane potentials. It appears likely that direct electrostrictive forces disrupted the vesicle membranes and facilitated their transition to stacked lamellar structures known as liposomes.

Retinal damage thresholds in the Maeaca fascicularis were determined for irradiation with single ultrashort pulses and entire pulse trains of 2nd harmonic light. In terms of irradiance at the retina, the fundoscopically determined 24-hr postexposure thresholds were  $4.4 \text{ mJ/cm}^2$  and  $540 \text{ mJ/cm}^2$  respectively. The peak electric fields in both cases were of the order of  $6-7 \times 10^5 \text{ V/cm}^2$ , as in the case of the vesicles. Disruption of the cellular membranes is suggested as the threshold damage mechanism. In addition, it is postulated that for pulse trains, irreversible damage occurs very early in the train, at the first pulse to attain or exceed the threshold electric field.

The corneas of the same primates used in the retinal studies were irradiated with 4th harmonic (265 nm) mode-locked pulse trains derived from the Nd:Glass laser. Fluorescein slit-lamp examinations at 24-hr post exposure revealed a damage threshold of  $8.2 \text{ mJ/cm}^2$ . All damage was confined to the corneal epithelium. It is postulated that photochemical processes such as coagulation or denaturation of nucleoproteins and nucleic acids govern the damage mechanism in this case.

## PREFACE

The authors are deeply indebted to Ms. Carroll Harris for her expert assistance with the primate eye irradiation studies. Ms. Harris carried out all the veterinary procedures and assisted in the evaluation of the retinal and corneal lesions. Thanks are also due to Mr. Nicholaus B. Martin for his assistance in the vesicle studies and to Dr. Oktay Yesil and Mr. Russell Tom for their technical assistance in the primate irradiation experiments. Finally, the authors are grateful to Dr. John Taboada, U.S. Air Force School of Aerospace Medicine, Laser Effects Branch, for carrying out the probit analyses reported here.

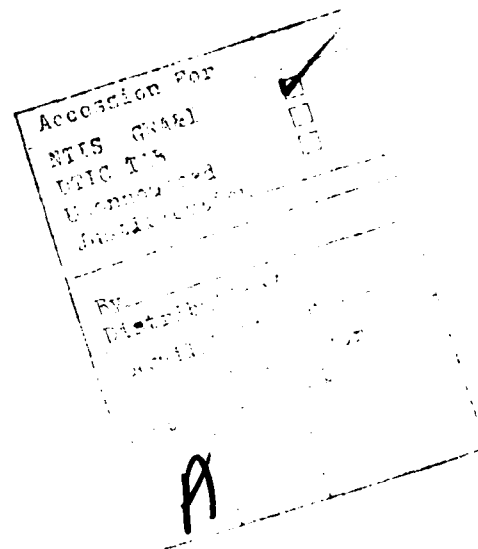


## TABLE OF CONTENTS

	<u>Page</u>
INTRODUCTION . . . . .	7
<u>PART I: MACROMOLECULAR DAMAGE STUDIES</u> . . . . .	10
REVIEW OF PRIOR WORK . . . . .	10
OBJECTIVES . . . . .	11
SEARCH FOR PICOSECOND OPTICAL STRESS-INDUCED DAMAGE IN DNA . . . . .	12
Instrumentation and Techniques for Studying Possible Damage to DNA . . . . .	12
Gel Electrophoresis . . . . .	12
Low-Shear Viscometry . . . . .	14
Dynamic Light Scattering . . . . .	15
Results of Damage Studies on DNA at 1060 nm . . . . .	15
Damage Studies of DNA Irradiated at 1060 and 530 nm Simultaneously . . . . .	18
Summary of DNA Damage Studies . . . . .	19
ATTEMPTS TO OBSERVE TRANSIENT DISTORTION BIREFRINGENCE OF DNA INDUCED BY PICOSECOND PULSES OF 1060-nm LASER LIGHT . . . . .	21
Theory of the Optical Kerr Effect in Liquids Comprised of Single Rigid Molecules . . . . .	21
Estimation of Molecular Parameters for CS <sub>2</sub> . . . . .	24
Theory of Induced Distortion Birefringence of DNA . . . . .	26
Attempts to Observe Transient Distortion Birefringence of DNA . . .	28
DAMAGE STUDIES OF LIPID BILAYER VESICLES . . . . .	31
Dipalmitoyl Phosphatidyl Choline (DPPC) . . . . .	31
Preparation of DPPC Vesicles . . . . .	31
Experimental Measurements on DPPC Vesicles . . . . .	33
Results . . . . .	35
Egg-Yolk Lecithin (EYL) Vesicles . . . . .	38
Preparation of EYL Vesicles . . . . .	38
Damage Studies of EYL Vesicles . . . . .	40
Summary of EYL Results . . . . .	44
Future Vesicle Work . . . . .	44

	<u>Page</u>
<u>PART II: PICOSECOND OCULAR DAMAGE STUDIES ON PRIMATES</u>	45
INTRODUCTION . . . . .	45
RETINAL DAMAGE THRESHOLDS INDUCED BY PICOSECOND 530-nm LIGHT PULSES . . .	46
Irradiation Apparatus . . . . .	46
Configuration Used for Pulse Train Studies . . . . .	46
Configuration Used for Single-Pulse Studies . . . . .	46
Apparatus Common to Both Configurations . . . . .	49
Experimental Protocol . . . . .	50
Results . . . . .	53
Comparison with Other Work . . . . .	57
CORNEAL DAMAGE THRESHOLDS INDUCED BY PICOSECOND 265-nm LIGHT PULSES . . .	59
Irradiation Apparatus . . . . .	59
Experimental Protocol . . . . .	62
Results and Discussion . . . . .	62
REFERENCES . . . . .	66
APPENDIX A: PICOSECOND LASER IRRADIATION FACILITY . . . . .	71
Nd:Glass Laser. . . . .	71
Pockel's Cell Pulse-Switching System . . . . .	74
Pulse Chronometer System . . . . .	75
Pulse Energy Measurement . . . . .	76
APPENDIX B: EXPERIMENTAL PROTOCOL FOR DNA STUDIES . . . . .	78
APPENDIX C: DYNAMIC LIGHT SCATTERING FACILITY . . . . .	79

#### List of Illustrations

##### Figure

1. Optical configuration for detection of picosecond birefringence from DNA base-pairs . . . . .
2. D vs.  $K^2$  plot for a sample with typical pulse-train irradiation of 600 mJ/cm<sup>2</sup> total energy density . . . . .
3. D vs.  $K^2$  for different preparations of EYL vesicles . . . . .
4. Schematic of apparatus for irradiation of primate eyes with entire trains of ultrashort 2nd harmonic (530 nm) pulses derived from a mode-locked Nd:Glass laser . . . . .
5. Schematic of apparatus for irradiation of primate eyes with single ultrashort 2nd harmonic (530 nm) pulses derived from a mode-locked Nd:Glass laser . . . . .
6. Schematic of macular exposure sites in M. fascicularis retina . . . . .

	<u>Page</u>
7. Schematic of apparatus for irradiation of primate eyes with ultrashort 4th harmonic (265 nm) pulse trains derived from a mode-locked Nd:Glass laser . . . . .	60
8. Schematic of exposure sites on <u>M. fascicularis</u> cornea . . . . .	63
A-1. Schematic of apparatus for picosecond laser irradiation of macromolecular systems . . . . .	72
A-2. Schematic of video detection and display system . . . . .	77
C-1. Experimental arrangement for dynamic light scattering . . . . .	80
C-2. Block diagram of digital clipped correlator . . . . .	82

#### List of Tables

##### Table

1. Summary of DNA irradiation experiments . . . . .	16
2. Summary of DNA irradiation experiments at higher energy densities. .	17
3. Summary of two-wavelength DNA irradiation experiments (1060 nm + 530 nm) . . . . .	20
4. Summary of DPPC vesicle irradiation experiments . . . . .	33
5. Apparent diffusion coefficients ( $D \times 10^8 \text{ cm}^2/\text{sec}$ ) of DPPC vesicles determined by dynamic light scattering . . . . .	36
6. Apparent diffusion coefficients of DPPC vesicles as functions of sample age . . . . .	37
7. Values of $D$ at various $K^2$ for EYL vesicles . . . . .	41
8. Polydispersity $\mu_2/\bar{r}^2$ at $\alpha=30^\circ$ and $\alpha=120^\circ$ for EYL vesicles . . . .	43
9. Retinal damage thresholds at 530 nm . . . . .	54
10. Comparison of threshold damage data for vesicles and retinas . . .	56
11. Comparison of present retinal thresholds with results of other investigations (24 hr post exposure) . . . . .	58

BIOLOGICAL DAMAGE THRESHOLD INDUCED BY ULTRASHORT FUNDAMENTAL, 2ND,  
AND 4TH HARMONIC LIGHT PULSES FROM A MODE-LOCKED Nd:GLASS LASER

INTRODUCTION

The effects of laser radiation on various biological systems have been studied extensively for several years (1-5). The eye has been found to be particularly susceptible to damage by exposure to radiation ranging from the ultraviolet (UV) to the infrared (IR) portions of the optical spectrum (1-3, 6-31). Depending on the wavelength of the laser radiation, ocular damage is most likely to occur in the cornea, the lens, or the chorioretinal tissues of the eye. The clear tissues of the eye are quite transparent in the visible and near IR (32); consequently, radiation in this wavelength range affects primarily the retina. In the UV the bulk of the incident radiation is absorbed in the anterior portion of the eye; below about 300 nm, the absorption occurs entirely in the cornea, usually within the corneal epithelium (2,25). It follows then that ocular damage from the visible and near IR is sustained primarily in the retinal tissues; while from the UV, it is sustained primarily in the corneal tissues.

The mechanisms responsible for UV-induced damage in the cornea are believed to be predominantly photochemical (25,27). However, relatively little work has been done on the ocular hazards of UV laser radiation, particularly in the ultrashort pulse regime and with respect to the effects of pulse duration in general.

By contrast, a large body of data exists on the effects of visible and near-IR laser radiation on the retina (6-24, 28-31). The bulk of the work has been carried out with CW or pulsed lasers of various wavelengths in the nanosecond or longer pulse duration regime. Until recently, relatively little attention was paid to the ocular hazards of ultrashort laser pulses ( $10^{-12}$  -  $10^{-11}$  sec) (28-31). For the longer pulse durations ( $>10^{-8}$  sec), the injury to the retinal tissue is believed to be caused by local temperature rise and resulting protein denaturation and enzyme inactivation. Typical threshold values of radiant exposure at the retina that cause observable lesions approach

$\sim 1 \text{ J/cm}^2$  as the exposure time is reduced to  $10^{-8}$  sec. In the picosecond regime, there is less agreement on the damage thresholds, and values as low as  $2 \times 10^{-3} \text{ J/cm}^2$  (30) and as high as  $2 \text{ J/cm}^2$  (28) have been quoted.

There is general agreement, however, that in the picosecond regime the tissue damage is not of thermal origin (4,28-31). Several possible damage mechanisms have been suggested, such as intense acoustic transients, direct breakdown in the bulk, multiphoton ionization, and free radical formation (4,24,28-31). Other possible mechanisms include direct electromagnetic field-induced stresses in the nucleic acids, proteins, and cell and vesicle lipid membranes (30,31,33,34).

Identification of specific damage mechanisms in living tissue is difficult because, unlike the optically pure samples used in inanimate material studies, biological materials are heavily concentrated with optical inclusions, free-charge regions, and dielectric absorption discontinuities. Furthermore, the end point resulting from energy deposition may be reached by a complicated set of pathological changes, with a result that is difficult to interpret. The important constituents of a living cell that are likely candidates for sites of radiation damage are its proteins, including fibrous structural and contractile proteins, enzymes, and other polypeptides; its nucleic acids, which are generally found in cells to be complexed with basic proteins (histones) in a form called chromatin, or complexed with polyamines; and, finally, its cell and vesicle lipid membranes (34).

We have approached this problem by (1) investigating the effects of ultra-short-pulse laser radiation on isolated biological macromolecular systems similar to constituents of living cells that are susceptible to damage and (2) comparing the results to data obtained from direct ocular damage experiments.

The first phase of the program described in this report was designed to study the effect of ultrashort pulses of 1060-nm light, and its 2nd harmonic, derived from a mode-locked Nd:Glass laser, on aqueous suspensions of macromolecular structures such as calf-thymus DNA, poly(L-lysine), DPPC vesicles, and egg-yolk lecithin vesicles. The experiments have encompassed a wide range of pulse energies for both single pulses and entire trains of mode-locked pulses. Particle damage has been monitored by one or more of the following techniques (depending on the particular macromolecule): dynamic light scattering, gel electrophoresis, and low-shear viscometry. In the case of DNA, which suffered

no damage detectable by these techniques at the energy densities attainable, we have also carried out a theoretical and experimental investigation of transient distortion birefringence to ascertain if any detectable internal strain is induced by the laser pulses.

The second objective of our program was to determine direct ocular damage thresholds in primates resulting from the 2nd harmonic (530 nm) and the 4th harmonic (265 nm) ultrashort-pulse radiation derived from the same laser, and to compare the results with those of the macromolecular studies, with a view to identify more closely the most likely damage mechanism(s). These studies were also aimed to help establish new laser safety standards in the picosecond time regime at these wavelengths.

This report is divided into two major sections: Part I deals with the macromolecular irradiation studies, and Part II treats the experimental determination of ocular damage thresholds in primate eyes.

## PART I: MACROMOLECULAR DAMAGE STUDIES

### REVIEW OF PRIOR WORK

Important macromolecular constituents of mammalian cells that are likely candidates for initial sites of ultrashort-pulse laser radiation damage are: (a) their proteins, including fibrous structural and contractile proteins, enzymes, and other polypeptides; (b) their nucleic acids, which are generally found in cells to be complexed with basic proteins (histones) in a form called chromatin, or complexed with polyamines such as spermidine; and (c) their noncovalent lipid membrane structures, including those of the outer integument, various vesicles, mitochondria, and other endoplasmic inclusions.

Work described in our previous technical report on this subject (34) indicated that the polypeptide poly(L-lysine) was unaffected by either single ultrashort pulses of 1060-nm laser light with energies up to  $1.37 \text{ mJ/cm}^2$  or successions of up to four pulse trains, each consisting of ~100 pulses and having integrated energy densities of up to  $150 \text{ mJ/cm}^2$ . It was inferred that polypeptides, or proteins, are unlikely to be the initial sites of any biological damage at these or lower energy densities.

The major effort of our previous investigations was to study the effects of ultrashort pulses of 1060-nm laser radiation on DNA. Three potential damage mechanisms were theoretically analyzed for their resulting distributions of fragment sizes. We concluded that a clear-cut distinction between damage mechanisms could in principle be made in the event that damage was unequivocally observed. Unfortunately for us, but perhaps fortunately for laser-damage victims, breakage of the DNA was unambiguously observed in only one sample, a result that we now strongly suspect was spurious. Most of the experiments revealed no detectable damage. Serious problems with both radiated and control DNA samples toward the end of the contract period resulted in a number of ambiguous experiments in which the DNA exhibited an anomalously high affinity for the Millipore filters, with consequent slow filtration and loss of sample and subsequent loss of precision in the dynamic light scattering measurements, which gave no positive indication of damage in any case. Because of these technical difficulties and because of the importance of observing

directly the fragment distribution, we undertook the development of a new analysis technique, gel-electrophoresis. However, final completion of the necessary apparatus and application of that technique to study irradiated DNA samples had to await the present contract period.

In summary, no detectable damage of DNA was produced by single pulses up to  $0.75 \text{ mJ/cm}^2$ , or two pulse trains up to  $230 \text{ mJ/cm}^2$  total energy density, or four pulse trains up to  $440 \text{ mJ/cm}^2$ . At higher total energy densities, the results were ambiguous due to technical problems. A primary objective of the present work has been to obtain unambiguous results for DNA irradiated at the highest obtainable total energy densities.

Some initial work was performed on the physical characterization of a preparation of purple membranes from Halobacterium halobium, which we hoped would provide a tractable model for a retinal membrane-protein system. Unfortunately, the ultrasonically dispersed suspensions of this material were neither as reproducible nor as stable as desired, so no irradiation experiments were undertaken.

#### OBJECTIVES

At the outset of the present investigations we intended to study DNA irradiated at the highest attainable energy densities--using dynamic light scattering, low-shear viscometry, and especially, gel electrophoresis--to detect any damage sustained and to analyze the distribution of product fragments. When it became clear that DNA was not detectably damaged by even the most energetic available laser pulses or whole trains of such pulses, we decided to investigate the transient distortion birefringence induced by such picosecond pulses. Our idea was that, even though rupture of covalent bonds was not observed, we might still be able to observe transient distortion induced by the high-power optical pulse; however, no transient distortion birefringence was ever observed.

When it became clear that the covalent bonds of both polypeptides and nucleic acids were unaffected by ultrashort pulses of 1060-nm light at the energy densities attained in these studies, we decided to focus our effort on noncovalent lipid membrane vesicles. Indeed, it was unambiguously and reproducibly observed that irreversible changes were induced in suspensions of di-palmitoyl phosphatidyl choline vesicles by trains of pulses with total energy densities exceeding  $600 \text{ mJ/cm}^2$ .

## SEARCH FOR PICOSECOND OPTICAL STRESS-INDUCED DAMAGE IN DNA

The quality control problems with the calf thymus DNA and/or filtration system that surfaced in the final phase of the early work have been essentially overcome by a combination of procedures, including

- (1) washing the filters in a hot solution containing 0.0115 M  $\text{Na}_2\text{CO}_3$  and 0.0015 EDTA, and
- (2) working with the DNA in a higher pH buffer, 1 M NaCl, 0.01 M EDTA, and 0.05 M  $\text{Na}_2\text{CO}_3$ , pH 9.3.

We do not understand why DNA passes through Millipore filters so much more easily at high pH ( $\geq 8.5$ ) than at neutral pH, but that has been a repeated observation in this laboratory.

Laser experiments with DNA at 1060 nm were performed following the protocol described in our previous report (34) with a somewhat modified laser system. Descriptions of the irradiation apparatus and experimental protocol are reproduced here in Appendixes A and B respectively. We temporarily removed the optics used for pulse chronography in order to increase the pulse energy available at the irradiation sample cell. The laser was operated multimode with the larger diameter laser beam focused down with a lens system to match the ID of the sample cell. This further increased the irradiation intensity. The beam profile, although not Gaussian, was free of large-scale intensity fluctuations (i.e., hot spots). Spatial intensity ripples were within 10% of the mean local intensity.

### Instrumentation and Techniques for Studying Possible Damage to DNA

Gel Electrophoresis--A gel electrophoresis apparatus was constructed using a J-wick flat-bed configuration designed for very dilute (0.5% or less) agarose gels. The entire unit was housed in a Lucite safety box with micro-switches in the latch to guarantee interruption of the high-voltage leads whenever the box was open. Considerable experimentation was done with methods of preparing, pouring, storing, loading, running, and developing the dilute agarose gels. Some of the most important guidelines to emerge from this activity were the following:

- (1) Agarose concentrations of at least 0.3% (w/V) were required to form gels strong enough to permit the necessary manipulation without breaking.
- (2) A "frame" several mm wide and 1-2 mm deep of more concentrated gel (1%) on the periphery was essential to provide adequate mechanical stability for manipulation of the more dilute bulk gel.
- (3) Interchanging the buffer in the anode and cathode compartments every few hours was effective in moderating pH drift.
- (4) Forming the gel on top of a removable plastic slab greatly facilitated the subsequent manipulations.

Typically, 10-20 microliters of solution containing 0.03-0.10 mg/ml DNA were loaded into one of the wells, or slots, on the "starting line" of a cold gel. These wells were impressions of the embedded teeth of a suspended comb remaining after the gel had cooled. The loaded wells were capped with a drop of warm agarose solution that was allowed to harden. The electrophoresis buffer that we have found works best, and gives the least pH drift, is 40 mM Tris (base), 1 mM NaEDTA, and 5 mM H<sub>3</sub>BO<sub>3</sub>. The voltage was initially set at 60 kV for 20-30 min until the DNA penetrated into the gel (from the well), then was maintained at 30 kV thereafter, which produced about 2 mA current. Bromthymol blue was added to one of the wells as a migration indicator. It moves with two to three times the speed of the native intact DNA. Typical run times were 18-24 hr. The gel slab was then removed from the apparatus and soaked in a solution containing ethidium bromide (~0.001 mg/ml) for 20-30 min. Then the gel was transferred to the illuminating upper surface of a UV black-light box. Ethidium cation fluoresces with a quantum efficiency about 200 x higher when bound to DNA than when free in solution, thus its bright orange fluorescence locates the position of the DNA "bands" in the gel. These bands could be photographed using an appropriate filter to block the exciting UV light. The resulting negatives could be scanned by densitometer to provide a very precise quantitative picture of the DNA distributions in the bands. Although this was done for a few runs, using equipment in the laboratory of W. Fangman, direct visual inspection generally sufficed to demonstrate that no damage was occurring. Therefore, densitometry was not further pursued, and that subject will not be discussed in the sequel.

At the time of writing, the total number of DNA samples analyzed by gel electrophoresis in this laboratory (for this and other projects) is well over

100. We have found that the technique is extraordinarily sensitive for detecting double-strand breaks, and practically, if not totally, insensitive to single-strand breaks. A surprising finding of our ongoing investigations of DNA was that even the internal motions manifested in the dynamic light scattering were completely insensitive to single-strand breaks at neutral pH (35). In fact, data in the older literature (36) indicate that the sedimentation coefficient and radius of gyration obtained from static light scattering, both of which monitor the bending rigidity, are insensitive to single-strand breaks at neutral pH. Thus, the insensitivity of the gel electrophoresis to single-strand breaks is consistent with these other observations. A recent discovery has shown that single-strand breaks, bound protein contaminants, and bound spermidine, can all induce profound changes in the Rouse-Zimm model internal motion parameters at pH 10.2 (37). These facts may be useful in any future DNA damage studies.

The presence of double-strand breaks, which we have often observed in samples contaminated with nuclease activity, is manifested by lower molecular weight components migrating, or streaking well ahead of the main band of the intact DNA. A simple description of the gel electrophoresis technique as applied to high molecular weight DNAs is given by Fangman (38).

Low-Shear Viscometry--A Crothers-Zimm-type rotating float viscometer with a shear of  $0.56 \text{ sec}^{-1}$  has been used to analyze irradiated DNA. The low-shear specific viscosity, as defined by

$$\eta_{sp} = \frac{\eta_{\text{solution}}}{\eta_{\text{solvent}}} - 1$$

is approximately proportional to  $M^{0.6-0.7}$ , where M = molecular weight, for a fixed weight concentration of DNA, and thus provides a rather sensitive indication of the average molecular weight in the sample (36). Considerable experimentation was required to evolve a procedure that would yield reproducible and reliable values of the accuracy required. Nutation of the float greatly perturbed the measured viscosities, and eventually was controlled only by altering the configuration of the rotating magnets, careful monitoring of the sample volume, and scrupulous attention to cleanliness.

The intrinsic viscosity  $[\eta] = \eta_{sp}/c = 60 \text{ dl/g}$  observed for the control is close to that expected for DNA molecules of molecular weight  $12 \times 10^6$ , which is what good samples of calf thymus DNA nearly always turn out to be.

Dynamic Light Scattering--The experimental instrumentation and techniques, including filtration procedures, were exactly as described in our recent report (34). (See also Appendix C.) This was by far the most difficult and time-consuming assay for damage, and was often fraught with problems believed to arise from dust inevitably present in the sample irradiation cells, which were very difficult to clean. Therefore, this technique assumed a secondary importance to the gel electrophoresis technique and was not run on all samples, especially those exhibiting significant dust problems.

#### Results of Damage Studies on DNA at 1060 nm

Table 1 presents the results obtained for five separate samples of the same calf-thymus DNA, which were exposed to picosecond pulse-envelopes ranging from a single pulse up to four pulse-trains, each containing the number of pulses indicated. The maximum energy densities are significantly higher than those reported previously. The differences in properties of the irradiated and control samples lie well within their respective experimental errors in all cases. The positions and widths of the gel electrophoresis bands of all the irradiated samples were identical to those of the control, as denoted by the "neg" result. There is clearly no significant fragmentation of DNA at these power levels under the present conditions.

The presence of unusually large amounts of dust and/or aggregates in these samples precluded accurate dynamic light scattering measurements, but the gel electrophoresis was fortunately unaffected by such contaminants. Interestingly, the occurrence of Tyndalls due to dust and/or aggregates diminished in the order in which the samples were introduced to the cell, suggesting strongly that the dust was initially present in the radiation cell, which was very difficult to adequately clean, and was gradually washed out by successive samples. The control, which was run last, was quite clean.

Table 2 presents results obtained for calf-thymus DNA at still higher energy densities. In fact, in sample 5 of that Table the incident beam was focused into the sample cell with a 55-mm-focal-length (f.l.) lens to cause dielectric breakdown in the DNA solution. The focal spot size in that case was ~55 μm. The sample was irradiated with two pulse trains and was repositioned after the first train so that breakdown would be produced at a different place in the cell. The occurrence of breakdown was evidenced by the generation of a greenish spark ~2 mm long and a sharp audible acoustic

TABLE 1. SUMMARY OF DNA IRRADIATION EXPERIMENTS

Sample	Irradiation	Energy density (mJ/cm <sup>2</sup> )	Shear viscometry [η](d <sub>1</sub> /g)	Apparent diffusion coefficient		Gel electrophoresis	Damage
				$\frac{D \times 10^8}{\theta = 25^\circ} \text{ cm}^2/\text{sec}$	$\frac{D \times 10^8}{\theta = 90^\circ} \text{ cm}^2/\text{sec}$		
1	1 pulse	3.85	-	1.15	3.45	Neg.	No
2	1 train 52 pulses	451	63.3	-	-	Neg.	No
3	1 train 102 pulses	502	-	-	-	Neg.	No
4	4 trains 1) 19 pulses 2) 43 " 3) N/A 4) 31 pulses	362 536 610 365	-	-	-	Neg.	No
5	4 trains 1) 86 pulses 2) 76 " 3) 87 " 4) 84 "	527 484 532 469	58.9	-	-	Neg.	No
6	Control sample	-	60.5	1.09	3.62	Neg.	-

Errors in [η] and D are several percent in each case.

TABLE 2. SUMMARY OF DNA IRRADIATION EXPERIMENTS AT HIGHER ENERGY DENSITIES

<u>Sample</u>	<u>Irradiation</u>	<u>Energy density (J/cm<sup>2</sup>)</u>	<u>Dynamic light scattering</u>		<u>Gel electrophoresis</u>	<u>Damage</u>
			<u>D × 10<sup>8</sup> cm<sup>2</sup>/sec</u>	<u>θ = 25°</u>	<u>θ = 90°</u>	
1	1 train	0.635	1.30	-	4.11	Neg.
2	1 pulse	6.85 × 10 <sup>-3</sup>	-	-	-	Neg.
3	1 train	2.16	1.36	4.00	Neg.	No
4	2 pulses (5.6 nsec apart)	1.7 × 10 <sup>-2</sup> 8.5 × 10 <sup>-3</sup>	1.28	3.98	Neg.	No
5	2 trains (breakdown)	4.55 × 10 <sup>3</sup> 4.42 × 10 <sup>3</sup>	1.44	-	-	No
6	Control sample	-	1.41	4.08	Neg.	--

transient. Maximum electric-field strengths in these focused pulse trains were about  $6 \times 10^9$  V/m. Again, both dynamic light scattering and gel electrophoresis indicate that there was no significant fragmentation of any of these irradiated DNA samples. In related noncontract research, we have found that the apparent translational diffusion coefficient  $D(\theta=25^\circ)$  is much more sensitive to DNA fragmentation by contaminating nucleases than is  $D(\theta=90^\circ)$ .

It may be concluded that there is no detectable fragmentation of DNA upon irradiation by single picosecond pulses of 1060-nm laser light with energy densities up to  $17 \text{ mJ/cm}^2$ , or pulse trains with energy densities up to  $2.16 \text{ J/cm}^2$ , or focused pulse trains with energy densities at focus up to  $4.5 \times 10^3 \text{ J/cm}^2$ , the latter being sufficient to produce local dielectric breakdown.

#### Damage Studies of DNA Irradiated at 1060 and 530 nm Simultaneously

Letokhov (39) has suggested that multistage excitation of DNA in solution to energy levels high enough to produce dissociation, or fragmentation, could be achieved by simultaneous irradiation with very intense ( $\sim 10^9 \text{ W/cm}^2$ ) picosecond ( $\sim 10^{-11} - 10^{-12} \text{ sec}$ ) pulses of one or more frequencies, either one of which is too low to photodissociate the molecule in a single quantum event. This viewpoint ignores the effects of anharmonicity in the vibrational manifold and assumes a 10-fold smaller relaxation rate (at high excitation levels) than the well-documented very rapid relaxation of energy among the numerous (coupled) nondissociative modes at high excitation levels of large molecules even in the gas phase (40). The availability of a great many more coupled modes to accept the energy in condensed phases will probably increase the power requirements for such multistep photofragmentation far above the value estimated by Letokhov. Nonetheless, we decided to investigate the effect of irradiation at 1060 nm and 530 nm simultaneously. Two 530-nm photons would be equivalent to one at 265 nm, close to the maximum of the DNA ultraviolet absorption band at 263 nm.

The experimental setup was similar to that used for the 1060-nm studies, except that the dichroic beamsplitter that normally separates the IR and green components was replaced with an uncoated-glass beamsplitter. Thus, the 2nd harmonic could reach the target cell. Relative measurements of IR and green pulse energy for two experiments yielded an SHG conversion efficiency of 3% in one case and 11% in the other. The DNA samples were contained in the 5-mm-ID x 20-mm quartz cells. The laser aperture was set at 8 mm and a

50-cm-f.l. lens was used to reduce the beam diameter to 5 mm. By measuring burn spots on Polaroid film at the location of the target cell, we determined that the diameter of the 2nd harmonic beam was about half that of the IR. This is due partly to the square-law harmonic generation and the different effective focal length of the focusing lens for the two different wavelengths.

Table 3 contains the results of these simultaneous (1060 nm + 530 nm) irradiation experiments. Again, it may be concluded that no fragmentation of the DNA was detected. Although sample 1 seems to be giving slightly higher apparent diffusion coefficients, its gel electrophoresis band was unequivocally negative. As was often the case, the presence of dust in these samples greatly reduced the accuracy and reliability of the dynamic light scattering results, especially at the lower angles.

#### Summary of DNA Damage Studies

Tables 1, 2, and 3 of this report and the Summary Table of our previous report (34) show that our data overwhelmingly indicate no detectable damage in irradiated DNAs under any conditions that we have studied. The sole experiment that indicated positive breakage has now been superceded by numerous experiments at much higher energy densities, all of which give unequivocal negative results. Therefore, that single result is now presumed to be spurious.

Numerous direct attempts to produce a damaged DNA similar to that observed in the spurious experiment by conceivable experimental errors, such as deliberately leaving residual chromic acid cleaning solution in the radiation cell, were unsuccessful. However, in the course of subsequent noncontract research, we have actually twice experienced similar damage in DNAs stored in dilute solution in our refrigerator, presumably a consequence of the rapid production of nucleases by contaminating cold-insensitive microorganisms. We are, therefore, strongly inclined to ignore that one experiment, and accept the obvious conclusion that irradiated DNAs suffer no damage detectable by our techniques at the energy densities attainable.

TABLE 3. SUMMARY OF TWO-WAVELENGTH DNA IRRADIATION EXPERIMENTS  
 (1060 nm + 530 nm)

Sample	Irradiation	Energy density		Apparent diffusion coefficient		Gel electrophoresis	Damage
		1060 nm	530 nm	25°	D × 10 <sup>8</sup> cm <sup>2</sup> /sec		
1	1 pulse train 1060 nm + 530 nm	536	121	1.54	2.25	2.91	4.07
2	1 pulse train 1060 nm + 530 nm	598	291	1.26	2.05	2.73	3.88
Control for 1 & 2				1.28	2.08	2.63	4.06
				Neg.	Neg.	--	--

## ATTEMPTS TO OBSERVE TRANSIENT DISTORTION BIREFRINGENCE OF DNA INDUCED BY PICOSECOND PULSES OF 1060-nm LASER LIGHT

One of the potential damage mechanisms for DNA conjectured in the previous report (34) was based on intramolecular strain caused by light-induced torques on the optically anisotropic DNA bases. Even though strain to the point of fragmentation did not occur, strain may still take place to a sufficient extent to produce a detectable birefringence. An experiment to test this hypothesis is worthwhile for several reasons. If observed, such an intramolecular strain might permit a rough estimate of the laser powers ultimately required for fragmentation. Also, if observed, the transient decay of the optically induced birefringence could provide new information regarding the dynamics of these macromolecules on the picosecond time scale. Even if not observed, it might be possible to set a useful lower limit on the restraining forces governing tilting of the DNA bases with respect to the helix axis, about which essentially nothing is known.

### Theory of the Optical Kerr Effect in Liquids Comprised of Single Rigid Molecules

In a liquid comprised of cylindrically symmetric nonpolar molecules with polarizability  $\alpha_0 = (\alpha_{11} + 2\alpha_{\perp})/3$  and anisotropy  $\Delta\alpha = \alpha_{11} - \alpha_{\perp}$ , the dipole moment ( $\mu_{zi}$ ) of the  $i$ th molecule induced by a z-polarized constant macroscopic electric field ( $E_z$ ) can be written in the form

$$\mu_{zi} = fE_z[\alpha_0 P_0(\cos \theta_i) + \frac{2}{3} \Delta\alpha P_2(\cos \theta_i)], \quad (1)$$

where  $\theta_i$  is the polar angle between the molecular symmetry axis and the electric field,  $P_r(\cos \theta_i)$  is the  $r$ th Legendre polynomial of  $\cos \theta_i$ , and  $f = E_{loc}/E_z$  is the internal field correction factor relating the local cavity field  $E_{loc}$  to  $E_z$ .

Interaction energy between the applied electric field  $E_z^0 = \epsilon E_z$  and the total induced polarization in the sample of  $N$  molecules in volume  $V$  is (41)

$$H(t) = - \int E_z^0 \cdot dP_z = - \frac{(E_z^0)^2}{2} f [N\alpha_0 + \frac{2}{3} \Delta\alpha \sum_j P_2(\cos \theta_j)]. \quad (2)$$

Neglecting the orientation independent part, and generalizing to the mean interaction energy with a very rapidly oscillating optical field (for which  $(E_z^0)^2/2 \rightarrow (E_z^0)^2/4$ ), this relation takes the canonical form of Kubo (42):

$$H(t) = -F(t) \cdot A = - \left[ \frac{(E_z^0)^2}{4} \right] \cdot f \left[ \frac{2}{3} \Delta\alpha \sum_j P_2(\cos \theta_j) \right], \quad (3)$$

where the second equality serves to define the quantities  $F(t)$  and  $A$ . The time-dependence of  $F(t) = (E_z^0)^2/4$  is assumed to be very slow compared to the optical frequency of the irradiating light.

Using the relations  $D_z = E_z + 4\pi P_z = \epsilon_z E_z$ ,  $n_z^2 = \epsilon_z$  (at optical frequencies), and  $n_z = n_0 + \delta n_z$ , it is readily found to lowest order in  $\Delta\alpha$  that

$$\delta n_z = \frac{4\pi}{3} \frac{f}{n_0} \frac{\Delta\alpha}{V} \sum_i P_2(\cos \theta_i) = B, \quad (4)$$

where the last equality serves to define  $B = \delta n_z$ .

From Kubo's fluctuation-dissipation theory (42), the linear response of  $B = \delta n_z$  to a sinusoidally varying  $F(t) = [(E_z^0)^2/4]\cos \omega t$  (where  $\omega$  is here understood to be much smaller than optical frequencies) is simply

$$B(t) = \text{Re}\{\chi_{BA}(\omega)\}F_0 \cos \omega t + \text{Im}\{\chi_{BA}(\omega)\}F_0 \sin \omega t, \quad (5)$$

where the real and imaginary parts of the susceptibility are given by

$$\text{Re}\{\chi_{BA}(\omega)\} = \frac{\langle AB(0) \rangle}{k_B T} - \frac{\omega}{k_B T} \int_0^\infty \langle AB(t) \rangle \sin \omega t dt \quad (6)$$

$$\text{Im}\{\chi_{BA}(\omega)\} = \frac{\omega}{k_B T} \int_0^\infty \langle AB(t) \rangle \cos \omega t dt. \quad (7)$$

Here  $T$  is the absolute temperature,  $k_B$  is Boltzmann's constant, and the angular brackets denote equilibrium averages for the system in the absence of the perturbing optical field.

For  $F(t)$  varying slowly compared to the rotational relaxation time (e.g., of  $\text{CS}_2$  in the present instance),  $\text{Im}\{\chi_{BA}(\omega)\} = 0$ , and  $\text{Re}\{\chi_{BA}(\omega)\} \approx \langle AB \rangle / k_B T$ . Thus the "steady state" (i.e.,  $\omega=0$ ) response of the refractive index to the perturbing optical pulse is

$$\delta n_z = \frac{(E_z^0)^2}{4} \frac{f^2}{k_B T} \frac{8\pi}{9} \frac{1}{n_0 V} \sum_{ij} P_2(\cos \varphi_i) P_2(\cos \varphi_j). \quad (8)$$

Now, using the identity  $P_2(\cos \varphi_i) = \sqrt{\frac{4\pi}{5}} Y_{20}(\varphi_i)$ , where  $\varphi_i = (\theta_i, \phi_i)$ , and  $Y_{20}(\varphi_i)$  is the corresponding spherical harmonic, one obtains

$$\langle P_2(\cos \varphi_i) P_2(\cos \varphi_j) \rangle = \frac{4\pi}{5} \langle Y_{20}(\varphi_i) Y_{20}(\varphi_j) \rangle = \frac{1}{5} \langle P_2(\hat{u}_i \cdot \hat{u}_j) \rangle, \quad (9)$$

where the last line follows from the addition theorem of spherical harmonics (43) and the fact that the liquid exhibits an isotropic equilibrium state. The  $\hat{u}_i$ ,  $\hat{u}_j$  are unit vectors directed along the symmetry axes of molecules i and j.

The instantaneous angular distribution of symmetry axes can always be expanded in the complete set of Legendre polynomials. It is apparent from Eq. 4 that  $\delta n_z$  must be proportional to the coefficient  $c_2(t)$  of the  $P_2(\cos \varphi)$  term, provided that  $c_2(t)$  vanishes in the equilibrium state and does not contribute to  $n_0$ , as in the case for isotropic fluids. Under the same conditions, still to lowest order in  $\omega$ , it is readily shown that  $\delta n_x = \delta n_y = -2\delta n_z$ . Thus, one obtains finally

$$\Delta n = \delta n_z - \delta n_x = 3\delta n_z \quad (10)$$

$$= \frac{2\pi(N)}{n_0 k_B T} \frac{2}{15} [f^2 \{1 + (N-1) \langle P_2(\hat{u}_i \cdot \hat{u}_2) \rangle\}] (E_z^0)^2,$$

where  $(E_z^0)^2$  is the square of the (peak) amplitude of the perturbing optical beam in vacuo. This formula differs from the standard formula applicable to dilute gas phase molecules,

$$\begin{aligned}\Delta n &= \frac{2\pi\bar{V} \Delta g \Delta\alpha C_g n_0}{15 n_0^2 k_B T} (E_z^0)^2, \\ &= \frac{2\pi(\frac{N}{V}) \Delta\alpha}{15n_0 k_B T} (E_z^0)^2\end{aligned}\quad (11)$$

by the appearance of the factor in square brackets. In Eq. 11,  $C_g$  is the concentration in  $\text{g/cm}^3$ ,  $\Delta g = \Delta\alpha/V_m$ , where  $V_m$  = molecular volume in  $\text{cm}^3$ , and  $\bar{V}$  = specific volume ( $\text{cm}^3$  per g); hence  $C_g (\bar{V}/V_m) = N/V$ .

The Clausius-Mosotti theory of the internal field gives

$$n_0 = \frac{3}{4\pi} \left(\frac{V}{N}\right) \frac{n_0^2 - 1}{n_0^2 + 2} = \frac{3}{4\pi} \left(\frac{M}{N_{Av} \rho}\right) \frac{n_0^2 - 1}{n_0^2 + 2}, \quad (12)$$

where  $M$ ,  $N_{Av}$ , and  $\rho$  are the molecular weight in daltons, Avogadro's number, and the density, respectively. The same internal field theory, which is known to be only approximate, gives

$$f = \frac{E_{loc}}{E_z} = \frac{n_0^2 + 2}{3}. \quad (13)$$

Unfortunately, the value of the orientation pair correlation function  $OPC2 = \{1 + (N - 1)\langle P_2(\hat{u}_1 \cdot \hat{u}_2)\rangle\}$  is not available for  $CS_2$ , and no simple theory is available for guidance. Values reported for chloroform and nitrobenzene are 2.0 and 2.8, respectively.

#### Estimation of Molecular Parameters for $CS_2$

For  $CS_2$  at  $25^\circ\text{C}$ , the Handbook of Chemistry and Physics gives a refractive index  $n_0 = 1.628$  and a density  $\rho = 1.595 \text{ g/cm}^3$ . Using these values in Eq. 12 above gives  $\alpha_0 = 6.7 \times 10^{-29} \text{ cm}^3$ . The value  $f = 1.55$  is estimated from Eq. 13.

The birefringence induced by high-power optical pulses has been found experimentally to obey the relation (44)

$$\begin{aligned}
 \Delta n &= 2.2 \times 10^{-20} \cdot (\text{volts/cm})_{\text{RMS}}^2 \\
 &= 2.0 \times 10^{-11} \cdot (\text{statvolts/cm})_{\text{RMS}}^2 \\
 &= 1.0 \times 10^{-11} (E_z^0)^2.
 \end{aligned} \tag{14}$$

Comparing this expression with Eq. 10 and using the values of  $n_0$ ,  $\alpha_0$ ,  $f$ , and  $N/V = \rho N_{\text{Av}}/M$  given above, yields finally

$$\Delta\alpha = \frac{7.25 \times 10^{-24}}{(\text{OPC2})^{\frac{1}{2}}} \text{ cm}^3. \tag{15}$$

The interesting difficulty here is that if OPC2 were of order 1.0, then  $\Delta\alpha$  would be comparable to, or even larger than, the estimated  $\alpha_0 = 6.7 \times 10^{-24} \text{ cm}^3$ . A second estimate of  $\alpha_0$  is available from the molar polarization  $(4\pi/3)N_{\text{Av}}\alpha_0 = 21.1 \text{ cm}^3/\text{mole}$  of  $\text{CS}_2$  dissolved in other nonpolar solvents, as tabulated by Debye (45). This datum gives  $\alpha_0 = 8.4 \times 10^{-24} \text{ cm}^{-3}$ , comparable to the previous value. One is forced to conclude that either  $\Delta\alpha$  or OPC2, or both, are much larger than expected. Typically  $\Delta\alpha \approx \alpha_{11} - \alpha_{\perp}$  is only a few percent of  $\alpha_0 = (1/3)(\alpha_{11} + 2\alpha_{\perp})$ . However, for  $\text{CS}_2$ , we must have  $\Delta\alpha/\alpha_0$  greater than 0.3 if OPC2 is less than 10!

The point of the above discussion is to note that  $\text{CS}_2$  provides an extraordinarily large induced birefringence due to either an enormously large  $\Delta\alpha$  in comparison to  $\alpha_0$  or to a very large equilibrium orientation pair correlation function, which implies that many  $\text{CS}_2$  molecules will orient cooperatively due to strong intrinsic orientational coupling among them, or to both effects. From a comparison of Eqs. 10 and 11, we see that the simple standard formula in Eq. 11 can be used if  $\text{CS}_2$  is assigned an apparent  $\Delta\alpha_{\text{app}}$  defined by

$$\begin{aligned}
 \Delta\alpha_{\text{app}} &\equiv \Delta\alpha(1.55) (\text{OPC2})^{\frac{1}{2}} \\
 &\approx 1.2 \times 10^{-23} \text{ cm}^3,
 \end{aligned} \tag{16}$$

where use has been made of Eq. 15. This apparent anisotropy substantially exceeds  $\alpha_0$  for the reasons cited above.

#### Theory of Induced Distortion Birefringence of DNA

An optical pulse of duration  $10^{-11}$  sec passes by too rapidly to effect significant reorientation of the helix-axis of DNA but may be able to tilt the base-pairs (which are regarded here as a single rigid unit) with respect to the helix-axis, thereby inducing some distortion birefringence.

Attention is focused on a single base-pair, which is imagined to have an optical polarizability that is cylindrically symmetric about the fixed local helix-axis in the undistorted configuration. That fixed helix-axis in turn makes an angle  $\theta$  with respect to the polarization vector  $\hat{z}$  of the optical pulse. If there were no distortion, the interaction energy of the single base-pair with the optical field would be given by the appropriate modification of Eq. 2 for a single molecule.

The orientation of the base-pair with respect to the helix-axis is governed by an angular harmonic restoring potential  $gn^2/2$ , where  $g$  is the restoring torque constant and  $n$  is the angle of deflection or tilt away from the equilibrium configuration. The equilibrium probability distribution for  $n$  is

$$P(n)dn = \frac{e^{-\frac{gn^2}{2k_B T}}}{\sqrt{2\pi k_B T/g}} dn. \quad (17)$$

The interaction energy between the optical pulse and the base-pair is

$$H(t) = -\frac{(E_z^0)^2}{4} f\{\alpha_0 P_0 + \frac{2}{3} \Delta\alpha P_2 [\cos(\theta - n)]\} \quad (18)$$

If  $g$  is sufficiently large, then  $n \ll 1$ . Direct expansion for small  $n \ll 1$  gives

$$P_2[\cos(\theta - n)] \approx (1-2n^2)P_2[\cos \theta] + \frac{n^2}{2} + 3n \cos \theta \sin \theta. \quad (19)$$

Because the helix-axes are held fixed, the system can respond to the optical pulse only by changing  $n$ . Thus, the interaction energy between the optical pulse and those degrees of freedom (i.e.,  $n$ ) that are free to respond is

$$H_n(t) = - \left[ \frac{(E_z^0)^2}{4} \right] \left[ \frac{2\Delta\alpha}{3} f \left\{ -2n^2 P_2[\cos \theta] + \frac{n^2}{2} + 3n \cos \theta \sin \theta \right\} \right] \\ = -F(t) \cdot A_n . \quad (20)$$

The change in refractive index induced by the pulse acting on this one base-pair is found from Eq. 4 in the form

$$\delta n_z = \frac{4\pi}{3} \frac{f}{n_0} \frac{\Delta\alpha}{V} P_2 [\cos(\theta - \eta)] . \quad (21)$$

Because the  $\theta$  value for a given base-pair is fixed, only that part of  $\delta n_z$  that varies with  $n$  will actually contribute to a  $\delta n_z$  induced by base-tilting. Therefore we keep only the lowest  $n$ -dependent terms

$$\delta n_z = \frac{4\pi}{3} \frac{f}{n_0} \frac{\Delta\alpha}{V} \left\{ -2n^2 P_2(\cos \theta) + \frac{n^2}{2} + 3n \sin \theta \cos \theta \right\} \\ = B_n . \quad (22)$$

Again, linear response theory may be employed with the result that the steady-state birefringence is given by

$$\delta n_z = \left[ \frac{(E_z^0)^2}{4} \right] \frac{\langle A_n B_n \rangle}{k_B T} \\ = \frac{(E_z^0)^2}{4} \frac{f^2}{k_B T} \frac{8\pi}{9} \frac{\Delta\alpha^2}{V} \langle \{-2n^2 P_2[\cos \theta] + \frac{n^2}{2} + 3n \sin \theta \cos \theta\}^2 \rangle , \quad (23)$$

where the angular brackets denote an average over  $n$  using the canonical distribution in Eq. 17. Odd powers of  $n$  average to zero, and fourth-order terms are neglected; so only the  $\langle n^2 \rangle = k_B T/g \ll 1$  terms contribute. It is assumed that we are in the stiff limit where  $g \gg k_B T$ . Consideration of a collection

of  $N$  independently tilting base-pairs can be accommodated by multiplying Eq. 23 by  $N$  and performing an angular average over the uniform distribution of helix-axis orientations  $\theta$ . The entire final contribution comes from the  $\langle (3n \sin \theta \cos \phi)^2 \rangle$  term, and is given by

$$\delta n_z = \frac{4\pi}{15} \frac{f^2}{g} \frac{\Delta\alpha}{n_0} \left(\frac{N}{V}\right) (E_z^0)^2. \quad (24)$$

Again,  $\Delta n = \delta n_z - \delta n_x = 3\delta n_z$ , so finally

$$\Delta n = \frac{4\pi}{5} \frac{f^2}{g} \frac{\Delta\alpha}{n_0}^2 \left(\frac{N}{V}\right) (E_z^0)^2, \quad (25)$$

which may be compared to Eqs. 10 and 11 for freely orienting species. It should be noted that Eqs. 24 and 25 apply only when  $g/k_B T \gg 1.0$ .

#### Attempts to Observe Transient Distortion Birefringence of DNA

Herring sperm DNA (Na salt), Type VII from Sigma Lot #67C-00251, was sheared and concentrated down to approximately 63 mg/ml using a french press at 12,000 psi, and then evaporating in a vacuum. The size of the sheared fragments was estimated to be roughly 200,000 daltons with an average diffusion coefficient  $D \approx 8.2 \times 10^{-8} \text{ cm}^2/\text{s}$ . Shearing was necessary to achieve such a highly concentrated solution. This was then used as the active medium in an optical Kerr effect streak shutter (46), as indicated in Figure 1. Unfortunately, no detectable birefringence of the DNA was ever observed with DNA as the active medium in this apparatus.

The intensity of the maximum transmitted signal appeared as a vertical deflection of 5 cm on the oscilloscope display. A deflection as small as 2 mm would have been readily observed. In addition, the probe beam intensity was increased 60-fold for the DNA experiment. Thus, the transmission sensitivity of the streak shutter was  $60 \times 50/2 = 1500$  times higher in the DNA experiment than for  $\text{CS}_2$ . Because the particular apparatus used in this streak shutter gives a transmitted intensity signal proportional to  $\Delta n^2$ , we may conclude that

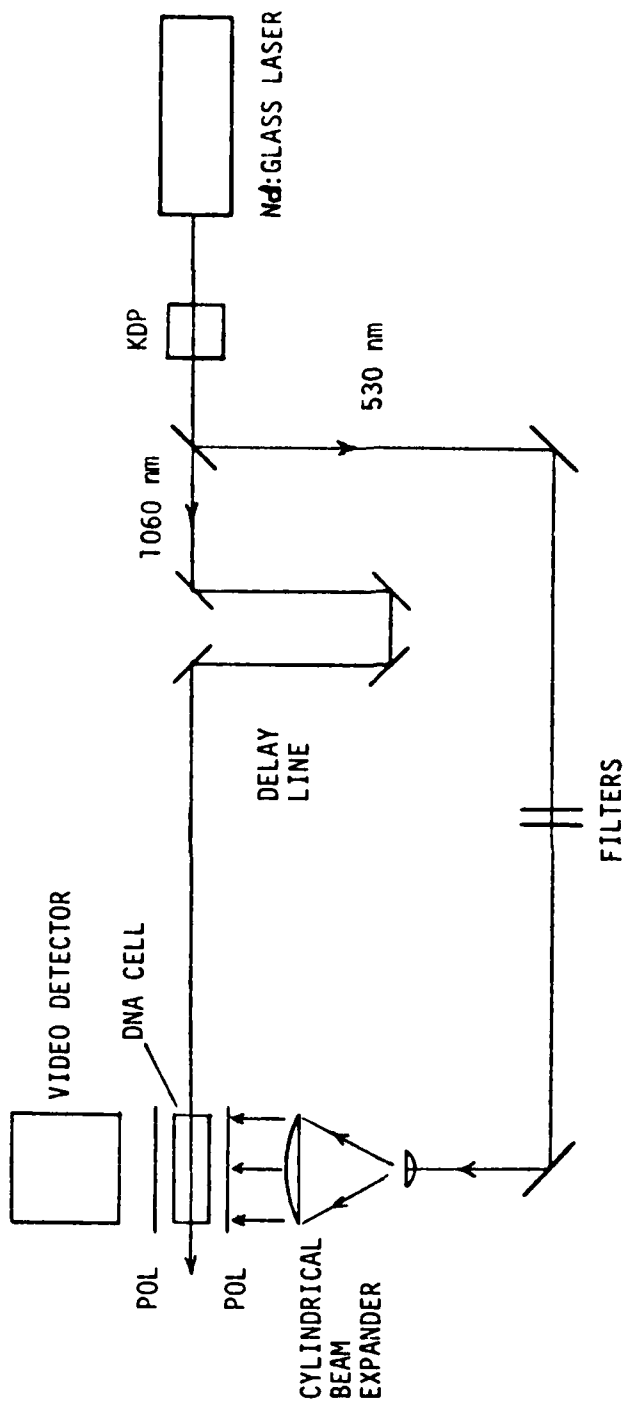


Figure 1. Optical configuration for detection of picosecond birefringence from DNA base-pairs.

$$\Delta n_{DNA}^{\max} < \frac{1}{\sqrt{1500}} \quad \Delta n_{CS_2}^{\max} = \frac{1}{38.7} \Delta n_{CS_2}^{\max}. \quad (26)$$

From the measured intensity of the gating pulse ( $I \sim 10^9 \text{ W/cm}^2$ ), the RMS volts/m can be recalculated and used in Eq. 14 to give  $\Delta n_{CS_2}^{\max} = 8 \times 10^{-5}$ . Thus,  $\Delta n_{DNA}^{\max} \lesssim 2 \times 10^{-6}$ .

A lower limit on the torque constant  $g$  can be obtained from Eq. 26 by using Eqs. 11 and 16 for  $\Delta n_{CS_2}^{\max}$  on the right-hand side, and Eq. 24 for  $\Delta n_{DNA}^{\max}$  on the left. That is,

$$\frac{4\pi}{5} \frac{f^2}{g} \frac{\tilde{\Delta\alpha}^2}{\tilde{n}_0} \left( \frac{\rho N_A v}{M} \right) (E_z^0)^2 \leq \frac{1}{38.7} \frac{2\pi}{15} \frac{1}{k_B T} \Delta\alpha_{app}^2 \left( \frac{\rho N_A v}{M} \right) (E_z^0)^2, \quad (27)$$

where the tilde (~) denotes quantities pertinent to the DNA solution. The parameters for  $CS_2$  were given earlier. For water,  $\tilde{n}_0 \approx 1.334$ , and Eq. 13 gives  $f = 1.26$ . For the DNA solution,  $\tilde{v} = 0.063 \text{ g/l}$ , and  $M = 662 \text{ per base-pair}$ . For one base-pair we take  $\Delta\alpha = -14.1 \times 10^{-24} \text{ cm}^3$ , which we have calculated from the flow birefringence data of Harrington (47) in 0.2 M NaCl, using his Eq. 2 together with the persistence  $a = 490 \text{ \AA}$  reported by Voordouw et al. (48). This value is slightly higher than that ( $\Delta\alpha = -12.9 \times 10^{-24} \text{ cm}^3$ ) computed by Harrington using  $a = 660 \text{ \AA}$ . Using these values, we obtain, finally, the lower limit

$$g \geq (3.23) k_B T = 1.32 \times 10^{-13} \text{ dyne-cm.} \quad (28)$$

This lower limit only marginally satisfies the inequality  $g \gg k_B T$  required for validity of Eqs. 20-25, and in that sense is disappointingly small. The torsion constant between base-pairs for the twisting of DNA has recently been measured (49) and found to be  $3.8 \times 10^{-12} \text{ dyne-cm}$ . Thus, this experiment has established only that the torque constant for base-tilting must exceed approximately 1/30 of the torsion constant for twisting successive base-pairs (about the helix axis) with respect to one another. That is neither a surprising nor a very useful result.

The same DNA preparation likewise showed no induced birefringence after being immersed in boiling water for 20 min (to denature the DNA) and then quenched in an ice bath.

We note that if the intensity of the orienting optical pulse could be increased by a factor of 10, then even a negative result would provide an interesting lower limit for the base-tilting torque constant.

#### DAMAGE STUDIES OF LIPID BILAYER VESICLES

##### Dipalmitoyl Phosphatidyl Choline (DPPC)

This synthetic pure lipid (i.e., DPPC) forms bilayer vesicle membrane structures by appropriate preparation, or introduction, in aqueous solution. It does exhibit a thermal order-disorder transition in the bilayer near  $T_m \approx 41^\circ\text{C}$ . The experiments reported here refer to vesicles at  $T < T_m$ , which exhibit the more ordered, less fluid phase of the membrane bilayer. They are, therefore, probably less representative of biological membranes, which are composed of a variety of mixed lipids for which the fluid phase is believed to prevail at room temperature. A few experiments performed subsequent to the contract indicate that the stability of DPPC vesicle suspensions is considerably reduced for  $T > T_m$ .

##### Preparation of DPPC Vesicles

Vesicles were prepared from a 95% ethanol solution of dipalmitoyl phosphatidyl choline (DPPC) at a concentration of 23  $\mu\text{mole}/\text{ml}$  (50). A 0.50-ml aliquot of the ethanolic lipid solution was injected into 10 ml of buffer (0.1 M NaCl and 0.01 M Tris-HCl) at a rate of 0.20 ml/min to give a final lipid concentration of 2.3  $\mu\text{mole}/\text{ml}$ . This injection method produced vesicles about 400  $\text{\AA}$  in radius, in good agreement with literature values (51). Some polydispersity existed even before irradiation, as evidenced by a decline in the apparent diffusion constant at low scattering angles ( $\theta \leq 45^\circ$ , or  $K^2 \leq 1.0 \times 10^{10} \text{ cm}^{-2}$ ), as shown in Figure 2. After exposure to picosecond laser radiation, the 2.3  $\mu\text{mole}/\text{ml}$  sample solution was transferred directly into a light scattering cell that had been previously rinsed free of dust by washing with filtered (0.2  $\mu\text{m}$  Millipore) buffer. The sample solution was diluted with filtered (0.2  $\mu\text{m}$ ) buffer to 0.23  $\mu\text{mole}/\text{ml}$  for use in dynamic light scattering (DLS).

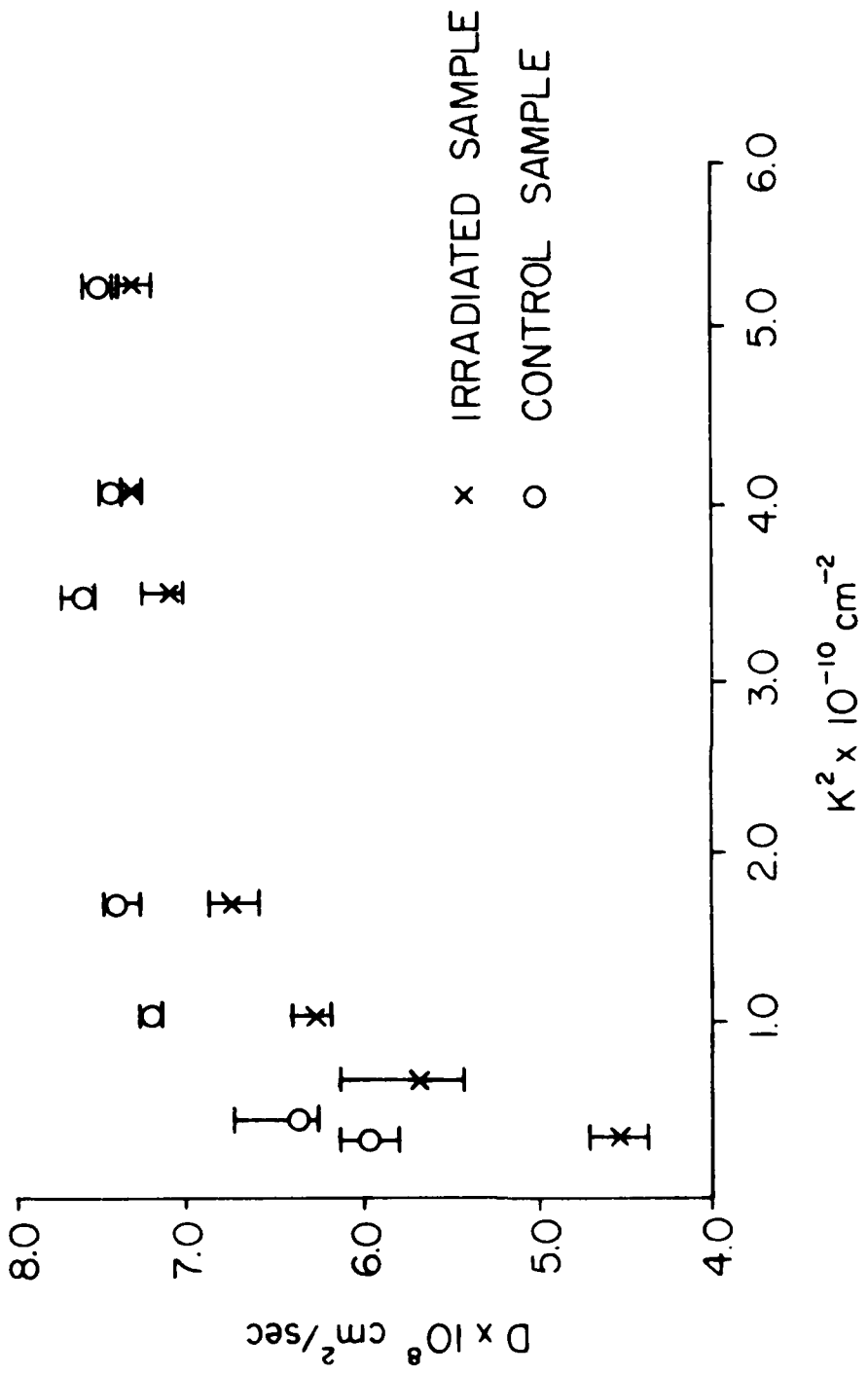


Figure 2.  $D$  vs.  $K^2$  plot for a sample with typical pulse train irradiation of  $600 \text{ mJ/cm}^2$  total energy density. Laser wavelength for dynamic light scattering is  $632.8 \text{ nm}$ . (Error bars indicate full range of measured  $D$  values.)

### Experimental Measurements on DPPC Vesicles

Nine successful exposures of the vesicles were carried out ranging from an energy density of  $9 \text{ mJ/cm}^2$  in a single pulse to  $3 \text{ J/cm}^2$  in an entire pulse train. The exposure parameters of the various samples are given in Table 4.

TABLE 4. SUMMARY OF DPPC VESICLE IRRADIATION EXPERIMENTS

<u>Sample</u>	<u>Irradiation</u>	<u>Energy density (mJ/cm<sup>2</sup>)</u>	<u>Damage</u>
1	pulse train	706	yes (massive)
2	1 pulse	9.0	possibly (slight)
3	pulse train	580	yes
4	pulse train	614	no
5	pulse train	3,080	yes (slight)
6	pulse train	529	no
7	pulse train	533	ambiguous (probably no)
8	pulse train	533	no
9	pulse train	529	no

Studies with DLS were performed on all of the samples as well as their appropriate controls. For a polydisperse solution of scatterers with dimensions small compared to  $K^{-1}$ , where  $K = (4\pi n/\lambda) \sin \theta/2$  is the scattering vector,  $n$  the index of refraction, and  $\theta$  the scattering angle. The apparent diffusion coefficient obtained from the dynamic light scattering is the so-called z-average value (52) defined by

$$D_z = \sum_i n_i m_i^2 D_i / \sum_j n_j m_j^2 , \quad (29)$$

where  $n_i$ ,  $m_i$ , and  $D_i$  are the number concentration, mass, and diffusion coefficient of the  $i$ th species. For spherical particles of dimension comparable to or larger than  $K^{-1}$ , the appropriate generalization of Eq. 29 is

$$D_{app} = \sum_i n_i m_i^2 P_i(K) D_i / \sum_j n_j m_j^2 P_j(K) , \quad (30)$$

where  $P_i(K)$  is the internal interference factor characterizing the  $i$ th species.  $P_i(K)$  decreases from a maximum value of 1.0 at small  $K^2$  to a lower value (depending on the particular shape and size of the scatterer) at any given larger value of  $K^2$ . For sufficiently large particles,  $P_i(K)$  is negligible at larger  $K^2$ , but at small  $K^2$  may permit the large particles to dominate the scattering from the smaller species, thus causing a decrease in the apparent diffusion coefficient at small  $K^2$  (as indicated in Fig. 2). Conversely, a significant decline in  $D$  at small  $K^2$  implies the existence of very large scatterers in the preparation.

The apparent Stokes radius  $R_h = k_B T / 6\pi\eta D$ --where  $k_B$  is Boltzmann's constant,  $T$  the absolute temperature,  $\eta$  the solution viscosity, and  $D$  the diffusion coefficient--was computed for the very large particles from the low-angle ( $25^\circ$  or  $30^\circ$ ) data for comparison with static light scattering measurements of the radii of gyration  $R_g$  of those same particles. The latter values were computed using the relation applicable for  $K^2 R_g^2 \leq 1.0$

$$I_N(\theta)/I_N(0) = 1 - K^2 R_g^2 / 3, \quad (31)$$

where  $I_N(\theta)$  is the "normalized" intensity (i.e., corrected for the relative size of scattering volume subtended at  $\theta$ ), and  $I_N(0)$  is the extrapolated value of  $I_N(\theta)$  at  $\theta = 0$ . A comparison of  $R_h$  and  $R_g$  values obtained for either radiated samples or controls over the mid- to low-angle range of measurements shows that  $R_g > R_h$  (typically,  $R_g \approx 1,600 \text{ \AA}$ ,  $R_h \approx 720 \text{ \AA}$ ), which implies a nonspherical, irregular or anisometric shape for particles of very large dimension, thus indicating that they are not simply very large spherical vesicles.

The ordinary vesicles ( $R_h \approx 450 \text{ \AA}$ ) do not satisfy the criterion,  $K^2 R_h^2 / 3 \geq 1$ , and hence do not produce sufficient variation in  $I_N(\theta)$  with  $\theta$  to yield a meaningful estimation of  $R_g$  using the present data. In experiments subsequent to the contract period, we have been able to obtain very precise static and dynamic light scattering data over the high  $K^2$  range ( $K^2 \approx 1 \times 10^{10} \text{ cm}^{-2}$ ;  $45^\circ \leq \theta \leq 120^\circ$ ) for somewhat larger vesicles, and have established that both  $R_h$  and  $R_g$  are consistent (within a few  $\text{\AA}$ ) with a spherical shell of outer diameter  $580 \text{ \AA}$  and thickness  $37 \text{ \AA}$ , the latter of which is the generally accepted value for lipid bilayers. The point of the latter remark is that we have now some hard evidence, for at least one preparation, that the actual shape of the ordinary vesicle species is close to spherical, as is widely believed.

Slow secular changes in the properties of all samples (including the nonirradiated controls) with time, required that the samples and controls be exposed and analyzed the very same day.

### Results

The criterion for assessing damage to the vesicles was whether the  $D$  vs  $K^2$  plots for the irradiated samples changed significantly in any respect when compared with their respective controls, which had not been subjected to picosecond laser radiation but otherwise had received identical handling, including loading into the irradiation cell. Both were observed at the same time.

Two regions of the  $D$  vs  $K^2$  curve are of special interest. The high-angle ( $\theta > 45^\circ$ ), or large  $K^2$ ,  $D$ -values give an indication of the z-average inverse hydrodynamic radii of the ordinary vesicles. The low-angle, or small  $K^2$ ,  $D$ -values contain primarily information about scattering centers of larger dimension, such as clumps of vesicles or large lamellar aggregates (liposomes) that scatter light predominantly in the forward direction.

Exposure of the vesicle suspensions to entire pulse trains with energy densities of  $600 \text{ mJ/cm}^2$  (peak electric field  $\sim 5.8 \times 10^5 \text{ V/cm}^2$ ) or greater did produce a distinct change in the  $D$  vs  $K^2$  curve, as indicated in Figure 2-- which shows that the apparent diffusion coefficient decreased by more than 25% at  $\theta = 25^\circ$  and by a smaller but still significant amount at higher angles. Our interpretation of this result is that the number and/or dimensions of the nonspherical aggregates, presumably multilamellar liposomes, have increased at the expense of the smaller ordinary vesicles destroyed by the light pulse.

Data for the various samples are summarized in a general way in Table 4. Values of the apparent diffusion coefficient observed at various angles are recorded in Table 5.

The massive damage sustained in sample 1, which was exposed to an entire pulse train, completely overshadowed the more modest changes in sample 2, which was exposed to a single pulse. However, after observing the behavior of the remaining samples, which include some samples of clear-cut negative results as well as some significant examples of more modest damage, including sample 3 (shown in Fig. 2), it seems possible that sample 2 actually sustained

TABLE 5. APPARENT DIFFUSION COEFFICIENTS ( $D \times 10^8$  cm $^2$ /sec) OF DPPC VESICLES DETERMINED BY DYNAMIC LIGHT SCATTERING

<u>Sample</u>	$\vartheta =$	<u>25°</u>	<u>30°</u>	<u>35°</u>	<u>45°</u>	<u>60°</u>	<u>90°</u>	<u>100°</u>	<u>120°</u>	<u>Damage</u>
1		0.452		0.833			3.81	4.40	4.86	yes
2		2.21	2.79	4.59			5.61		5.86	possibly
Control for 1 & 2		2.90	3.65	4.22	4.86	5.60	5.49	5.89		
3		4.53	6.24	5.69	6.29	6.75	7.13	7.36	7.29	yes
4		5.82	6.46			7.29	7.45		7.55	no
Control for 3 & 4		5.98	6.43		7.20	7.37	7.62	7.43	7.48	
5		1.40	2.08		4.23	4.73	5.07		5.41	slight
Control for 5		2.09	2.87		4.31	4.68	5.01		5.28	
6		3.05	3.64		4.78	5.00	5.44		5.76	no
7		2.50	3.65		4.56	4.89	5.34		5.48	prob. no
Control for 6 & 7		3.07	3.59		4.62	5.10	5.58		5.74	
8		3.32	3.65		4.83	5.05	5.51		5.79	no
9		3.32	3.83		4.82	5.12	5.53		5.80	no
Control for 8 & 9		3.44	3.97		4.70	5.09	5.43		5.67	

some significant damage after all. The pulse energy of  $9 \text{ mJ/cm}^2$  in that single pulse corresponded to a peak electric-field strength (assumed uniform over a 10-psec pulse) of  $\sim 7.1 \times 10^5 \text{ V/cm}$ .

Curiously, sample 5, which was exposed to an entire pulse train at very high energy density, showed rather slight indication of damage in the sense that there was a decrease in D only at small  $K^2$ , none at large  $K^2$ . However, that difference between the irradiated sample and control persisted into the second day after exposure, as indicated in Table 6, thereby increasing our confidence in that result. That sample was irradiated in the longer, narrower bore cell to achieve the higher energy density. These vesicles are known to stick to glass, and the large increase in surface area may have "fractionated" the irradiated sample in an unknown way.

TABLE 6. APPARENT DIFFUSION COEFFICIENTS OF DPPC VESICLES AS FUNCTIONS OF SAMPLE AGE

$(D \times 10^8 \text{ cm}^2/\text{sec})$

<u>Sample</u>	<u>Age</u>	<u><math>\theta = 25^\circ</math></u>	<u><math>\theta = 90^\circ</math></u>	<u><math>\theta = 120^\circ</math></u>	<u>Damage</u>
3	day 1	4.53		7.29	yes
	day 2	1.49		6.90	
4	day 1	5.82		7.55	no
	day 2	4.97		7.22	
5	day 1	1.40	5.07		slight
	day 2	0.932	4.72		
Control for 5	day 1	2.09	5.01		
	day 2	1.21	5.12		

These results indicate an approximate damage threshold of about  $600 \text{ mJ/cm}^2$  for DPPC vesicles exposed to trains of picosecond pulses of 1060-nm radiation. In addition, there is some indication that more modest damage might be inflicted by single picosecond pulses with an energy density of  $9 \text{ mJ/cm}^2$ . It is possible that electrostrictive or other forces present during the pulse actually rupture the vesicle every time, but that substantial recovery occurs between pulses in these systems. Certainly, vesicle fragments do not move far in  $10^{-9} \text{ sec}$ , and lipids are insoluble in aqueous solution. Thus, the observed damage may be minimal unless the vesicle is subjected to repeated battering by closely spaced pulses, as in a pulse train. In a system where chemical potential gradients and osmotic pressure differences exist across membrane, as

in living systems, a single rupture might lead to complete destruction of the osmotically strained vesicle, so the damage threshold in terms of peak electric field might be the same for single pulses and whole pulse trains in that case. Indeed, our studies of damage thresholds in primate retinae support this hypothesis. (See Part II of this report.)

It is also evident from Table 6 that the differences between samples 3 (damaged) and 4 (undamaged) persist into the second day after exposure, despite the long-term changes in both samples. Again, this argues that the differences between these samples are genuine.

The possibility of a thermal damage mechanism playing a role in the above experiments can be unequivocally ruled out--the temperature rise in our samples, as estimated from the difference in energy between the incident and the transmitted pulse trains, was less than  $0.02^{\circ}\text{C}$ .

#### Egg-Yolk Lecithin (EYL) Vesicles

Our results for DPPC vesicles apply to the ordered low-T phase of the membranes prevailing below  $T_m \approx 41^{\circ}\text{C}$ . The question naturally arises whether similar results would be found for membranes comprised of natural lipids, such as egg-yolk lecithin (EYL). Although both lipids are phosphatidyl cholines, the DPPC has two identical saturated 18-carbon fatty acid chains esterified to the glycerol moiety, whereas EYL phosphatidyl cholines generally contain a saturated fatty acid esterified at the 1 position in addition to the unsaturated fatty acid (usually oleic) at the 2 position. As a result of this chemical difference, and also the mixture of phosphatidyl cholines present, the EYL membranes exhibit a broad thermal transition between  $-15^{\circ}$  and  $-7^{\circ}\text{C}$  and are believed to exist in the fluid phase at room temperature,  $\sim 20^{\circ}\text{C}$ .

#### Preparation of EYL Vesicles

Considerable experimentation with parameters governing the vesicle preparations was conducted. The effects of mixing-temperature, initial concentration, needle gauge, and injection speed were all investigated. The  $D$  vs  $K^2$  curves for some of the resulting suspensions are indicated in Figure 3. The final procedure is described below.

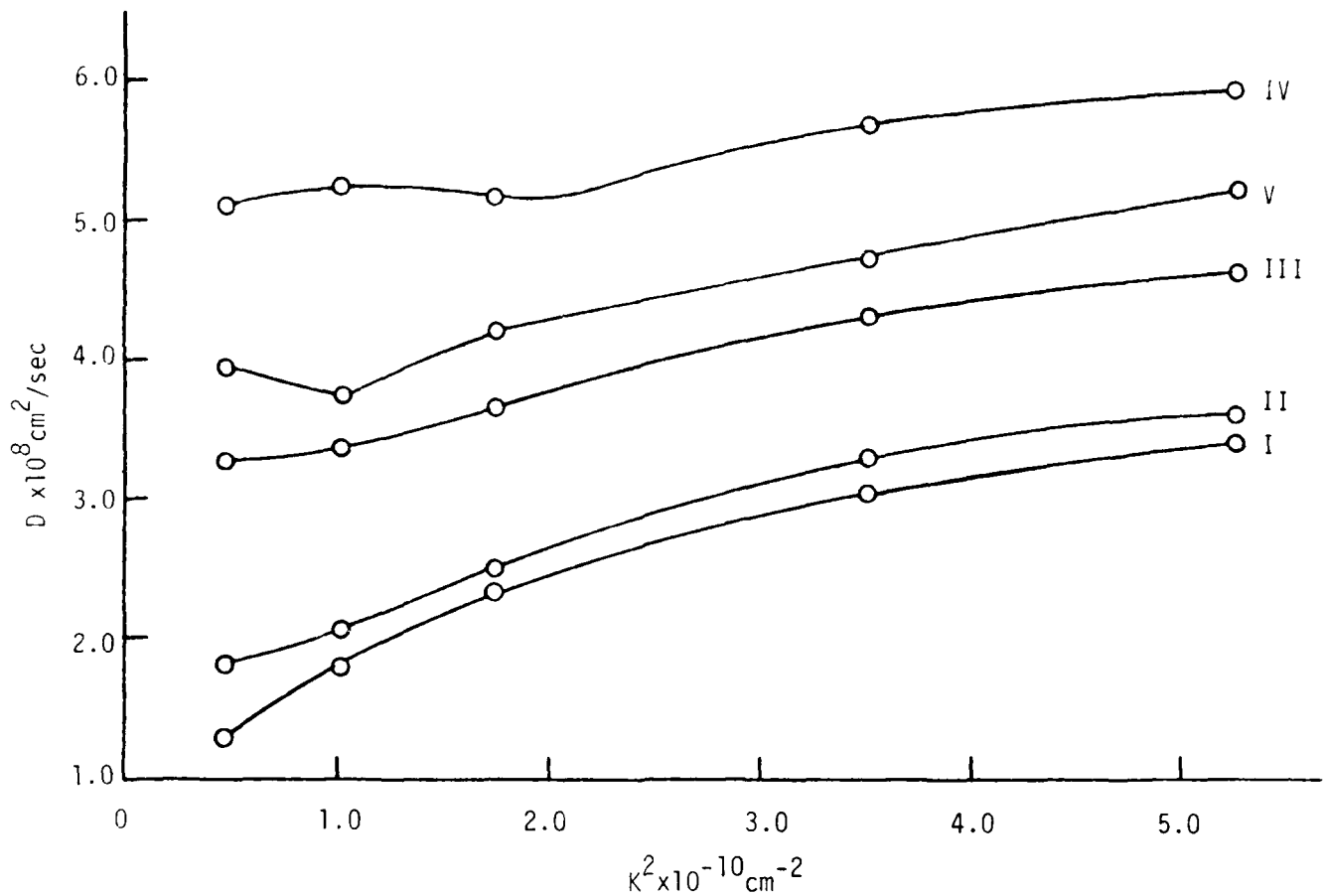


Figure 3.  $D$  vs.  $K^2$  for different preparations of EYL vesicles.

Prep. I. Step 1 (see text for steps) of the procedure was modified as follows: Inject 0.94 ml of 10 mg/ml stock into warm ( $40^\circ\text{C}$ ) buffer. Step 3 is omitted.

Prep. II. Step 2 was modified by injecting into warm ( $40^\circ\text{C}$ ) buffer. Step 3 was omitted.

Prep. III. Step 2 was modified by injecting into warm ( $40^\circ\text{C}$ ) buffer.

Prep. IV. Step 2 was modified by using 0.94 ml of 10 mg/ml stock.

Prep. V. Same as step 4.

For EYL commercially supplied in ethanolic solution, the following steps are carried out:

- (1) Rinse out a 25-ml flask and flush with filtered (0.22- $\mu\text{m}$  Millipore) buffer, leaving the magnetic stirring rod in the buffer solution to be rinsed at the same time.
- (2) Withdraw 0.5 of 10 mg/ml stock solution (95% ethanol), allow it to warm up for several minutes in syringe, then slowly inject into a 25-ml flask containing 10 ml of filtered (0.22- $\mu\text{m}$  Millipore) buffer. Use a Hamilton 1-cc syringe with a 22-gauge needle. The concentration in the flask is now 0.47 mg/ml.
- (3) Filter the suspension through 3.0- $\mu\text{m}$  Millipore filters twice.
- (4) Clean out scattering vessel with 0.22- $\mu\text{m}$  filtered buffer. Transfer 0.45 ml of solution into cell and dilute with 9 ml of clean buffer. Final concentration is 0.22 mg/ml lipid.

For lyophilized EYL make a 10 mg/ml solution in 95% ethanol first, then follow steps 1-4 above.

The buffer used for all experiments was 0.1 M NaCl + 0.01 M Tris (Sigma Trizma-base MW 121.1) titrated with HCl to pH 7.0.

The D vs  $K^2$  curves in Figure 3 show no limiting plateau at high  $K^2$ , which indicates a greater degree of polydispersity than found for DPPC vesicles.

#### Damage Studies of EYL Vesicles

EYL vesicles were exposed to mode-locked 1060-nm laser pulse trains with energy densities between 400 and 660 mJ/cm<sup>2</sup>. The results of dynamic light scattering measurements on the irradiated samples and corresponding identically treated controls are presented in Table 7. Although samples 6, 7, and 8, irradiated at the higher energy densities (657, 652, and 614 mJ/cm<sup>2</sup> respectively), exhibit D values marginally smaller than those of the controls at every angle, the data are not sufficiently different to warrant a definitive conclusion that damage occurred.

Unfortunately, all exposures at energy densities exceeding 600 mJ/cm<sup>2</sup> were obtained by decreasing the beam diameter by 20%, so not all of the sample solution was exposed to the full power of the irradiating beam. This practice was necessitated by the comparatively low energy output of the laser even with all operating parameters optimized.

Although the D vs  $K^2$  curves differed only marginally from the controls for the most intensely exposed samples, it is still possible that greater differences were manifested in the time-course of the decay of the correlation

TABLE 7. VALUES OF D AT VARIOUS  $K^2$  FOR EYL VESICLES  
 $D \times 10^8$  (cm/sec)

Sample	E (mJ/cm <sup>2</sup> )	$K^2 = 0.47 \times 10^{10}$	$K^2 = 1.03 \times 10^{10}$	$K^2 = 1.75 \times 10^{10}$	$K^2 = 3.51 \times 10^{10}$	$K^2 = 5.26 \times 10^{10}$
1	400	3.68	4.32	4.89	5.72	6.14
2	420	3.51	4.03	5.07	5.79	6.18
Control		3.92	4.40	5.11	5.81	6.22
3	420	3.39	4.40	4.97	5.45	5.91
4	516	3.05	4.17	4.94	5.48	5.88
Control		3.51	4.16	4.73	5.60	6.03
5	434	3.20	3.89	4.49	5.03	5.48
6	651	3.10	3.82	4.35	4.88	5.29
Control		3.18	3.98	4.39	5.09	5.46
7	652	3.15	4.01	4.52	5.01	5.43
8	614	3.02	3.80	4.37	4.90	5.27
Control		3.27	4.09	4.63	5.07	5.57

function. That is, the quality of single-exponential fit may still have varied significantly between irradiated samples and controls. A method for quantitatively measuring this deviation from single-exponential decay is that of cumulant analysis.

The normalized intensity autocorrelation function  $g^{(2)}(\tau)$  is a 4th-order correlation in the scattered electric field. Under the assumption of a Gaussianly distributed scattered field,  $g^{(2)}(\tau)$  may be related to the 2nd-order correlation function  $g^{(1)}(\tau)$  by (52)

$$g^{(2)}(\tau) = 1 + \beta |g^{(1)}(\tau)|^2 \quad (32)$$

where  $\beta$  is of order 1. If, furthermore, the sample is polydisperse,  $g^{(1)}(\tau)$  is weighted by the relative intensity distribution of scatterers  $G(\Gamma)$  with different decay constants  $\Gamma = K^2 D$ ,

$$|g^{(1)}(\tau)| = \int_0^\infty G(\Gamma) e^{-\Gamma\tau} d\Gamma \equiv \langle e^{-\Gamma\tau} \rangle \quad . \quad (33)$$

The exponential may be written in the form

$$e^{-\Gamma\tau} = e^{-\bar{\Gamma}\tau} e^{-(\Gamma-\bar{\Gamma})\tau},$$

where

$$\bar{r} \equiv \int_0^{\infty} G(r)r dr . \quad (34)$$

The factor  $e^{-(r-\bar{r})\tau}$  may be expanded and inserted in Eq. 33 with the following result:

$$|g^{(1)}(\tau)| = e^{-\bar{r}\tau} \left( 1 + \frac{\tau^2}{2!} \mu_2 - \frac{\tau^3}{3!} \mu_3 + \dots \right) , \quad (35)$$

where

$$\mu_2 \equiv \int G(r)(r-\bar{r})^2 dr$$

$$\mu_3 \equiv \int G(r)(r-\bar{r})^3 dr .$$

Thus, the intensity autocorrelation function may be expressed in terms of the moments of  $G(r)$ . It is then easily seen that (52)

$$\frac{1}{2} \ln[g^{(2)}(\tau) - 1] \doteq \frac{1}{2} \ln \beta - \bar{r}\tau + \frac{\tau^2}{2!} \mu_2 - \frac{\tau^3}{3!} \mu_3 + \dots \quad (36)$$

where use has been made of the expansion

$$\ln(1+z) = z - z^2/2 + \dots$$

Equation 36 is a polynomial in time whose coefficients are the moments of the distribution  $G(r)$ . The polydispersity of a sample of scatterers is here defined as the ratio of the second moment to the square of the average, that is,

$$\text{polydispersity} = \mu_2 / \bar{r}^2 .$$

A program was written to analyze certain sample runs according to the above polynomial. The algorithm first subtracts a baseline from the raw auto-correlation data. This baseline is first taken to be either the average of

the last 25 points or the baseline resulting from a single-exponential fit. Then the algorithm takes the natural logarithm, does a least-squares fit to the polynomial, and calculates  $\chi^2$ , the sum of the residuals, which is compared with the previous  $\chi^2$ . The baseline is varied until a minimum in  $\chi^2$  is obtained. The corresponding values of  $2\bar{r}$ ,  $u_2$ ,  $(2\bar{r})^{-1}$ , and polydispersity ( $u_2/\bar{r}^2$ ) are printed on the teletype.

The polydispersities obtained for correlation functions at small scattering angles ( $\theta=30^\circ$ ) always give higher values than at  $\theta=120^\circ$ , as shown in Table 8. The high-angle polydispersities were generally quite similar (i.e., within 10%) for the irradiated samples and their respective controls, whereas the polydispersities at  $\theta=30^\circ$  usually were substantially larger (by a factor ~1.8) for the irradiated samples than for controls, as also shown in Table 8. Thus, the cumulant analysis indicates an appreciable change in the irradiated samples studied (at  $435 \text{ mJ/cm}^2$  and  $650 \text{ mJ/cm}^2$ ) with respect to their controls. Unfortunately, this change was not consistently manifested. Moreover, cumulant analysis has some inherent weaknesses. The final results are inordinately sensitive to the value of the subtracted baseline, because the minimum in  $\chi^2$  with respect to baseline is not always unique. Moreover, as the value of the baseline was varied, the number of data points to be fitted also changed to prevent a zero or negative argument of the logarithm. This latter feature had the consequence that the fitting algorithm in some cases simply slid progressively to higher baselines with ever-fewer data points without converging to any local minimum in  $\chi^2$ .

TABLE 8. POLYDISPERSITY  $u_2/\bar{r}^2$  AT  $\theta = 30^\circ$  AND  $\theta = 120^\circ$   
FOR EYL VESICLES

	Sample 5 <u>435 mJ/cm<sup>2</sup></u>	Sample 6 <u>650 mJ/cm<sup>2</sup></u>	Control
$\theta = 30^\circ$			
$K^2 = 0.47 \times 10^{10}$	0.233	0.200	0.127
$\theta = 120^\circ$			
$K^2 = 5.3 \times 10^{10}$	0.125	0.117	0.130
Ratio (30/120)	1.86	1.71	1.02

### Summary of EYL Results

The EYL lecithin vesicles proved considerably more intractable than DPPC vesicles in every regard from preparation to analysis of their dynamic light scattering autocorrelation functions. Although some evidence of optical stress-induced changes, especially in the polydispersity parameter, was observed in some preparations, we feel that the evidence overall is too slim to warrant at this time an unequivocal statement concerning damage of these vesicles.

### Future Vesicle Work

The next logical step is to examine the susceptibility to picosecond laser pulses of osmotically strained vesicles; for example, containing concentrations of salt inside differing from those prevailing outside. In that case, which corresponds more closely to living organisms, one has the possibility that a single rupture event will be amplified to complete vesicle destruction by the osmotic gradient, with less likelihood of recovery. In such a case the damage threshold for single pulses could well approximate  $1/N$  of that for entire pulse trains, where  $N$  is the total number of pulses in the train. In other words, the first pulse to reach the threshold field would destroy the vesicles, and all subsequent pulses in the train would simply add "insult to injury."

## PART II: PICOSECOND OCULAR DAMAGE STUDIES ON PRIMATES

### INTRODUCTION

This phase of the program was designed to determine ultrashort pulse-induced ocular damage thresholds in the primate Macaca fascicularis\* at two different wavelengths, 530 and 265 nm, obtained by frequency upconversion of the Nd:Glass laser output, and to compare the effects of single pulses and entire mode-locked pulse trains at the 530-nm wavelength. In the visible spectrum the cornea, lens, and vitreous are highly transparent and thus damage is sustained in the chorioretinal region, whereas at the UV wavelength the incident radiation is absorbed mostly within the corneal epithelium.

The irradiation apparatus used in both the retinal and corneal damage studies was similar to that used in the macromolecular exposure experiments. (See Appendix A.) The output of the Nd:Glass laser was frequency-doubled to generate 530-nm light for the retinal damage studies and frequency-quadrupled to generate 265-nm radiation for the corneal threshold experiments. Additional details are given in the following sections.

The experimental protocol, parameters, and criteria we used followed as closely as possible those used in the bulk of previously published work, in order to permit direct comparisons with data acquired in prior research by other investigators.

We describe first the retinal damage threshold studies, which comprise two separate bodies of experimental data: (1) damage thresholds for entire mode-locked pulse trains, and (2) damage thresholds for single ultrashort pulses. The corneal ultraviolet irradiation experiments are discussed in the final section of this report.

\*Originally we planned to use rhesus monkeys (Macaca mulatta); however, the continuing embargo on the exportation of this species by India and the resulting severe shortage dictated the use of M. fascicularis. The structure and pigmentation of the retinae of the two species are very similar, allowing direct comparison of the present work with past results.

## RETINAL DAMAGE THRESHOLDS INDUCED BY PICOSECOND 530-nm LIGHT PULSES

### Irradiation Apparatus

The irradiation apparatus used in these studies had two somewhat different configurations: the first designed for experiments using the entire mode-locked pulse train of ~100 pulses, and the second for work using a single pulse selected from near the beginning of the pulse train.

Configuration Used for Pulse Train Studies--A schematic of the apparatus is shown in Figure 4. The infrared pulse train was frequency-doubled to 530 nm in a Type I phase-matched KD\*P crystal angle-tuned for maximum conversion efficiency (~12%). The 530-nm component was separated from the 1060-nm light by a dichroic beamsplitter (DBS). A Schott KG-3 filter blocked residual IR from the green beam. A half-wave retardation plate ( $\lambda/2$ ) rotated the polarization of 2nd harmonic light from the vertical to the horizontal plane. An uncoated pellicle beamsplitter ( $PL_1$ ) sampled a small fraction (~1.7%) of the green beam for pulse chronometry. The green pulse train was attenuated to approximately the desired energy level by a neutral density filter stack ( $NDF_1$ ). An Iris diaphragm (ID) selected the central 3 mm from the green beam, which had diverged to a diameter of ~10 mm at the location of this aperture.

The 2nd harmonic pulse energy was monitored by a Laser Precision RkP-331 pyroelectric energy probe calibrated by the manufacturer using standards traceable to the National Bureau of Standards. The pulse energy was sampled by an uncoated fused-silica beamsplitter (BS, total reflection coefficient = 7%, both faces), and focussed by a 15-cm-f.l. fused-silica lens into the aperture of the probe. The energy in the pulse train was displayed on a Laser Precision RkP-3230 digital readout unit.

Additional beam attenuation was provided, when desired, by a set of calibrated fused-silica neutral density filters ( $NDF_2$ ).

Configuration Used for Single-Pulse Studies--The setup used for single-pulse irradiation was somewhat different from that described above. (See Fig. 5.) First, the Pockels cell pulse-selecting system, installed ahead of the 2nd harmonic generator, was activated as described in Appendix A. Because of the low energy per pulse (~1% of the total energy in the pulse train), the half-wave retardation plate ( $\lambda/2$ ) was placed downbeam from pellicle  $PL_1$ . This increased the reflection coefficient of the pellicle by about an order of

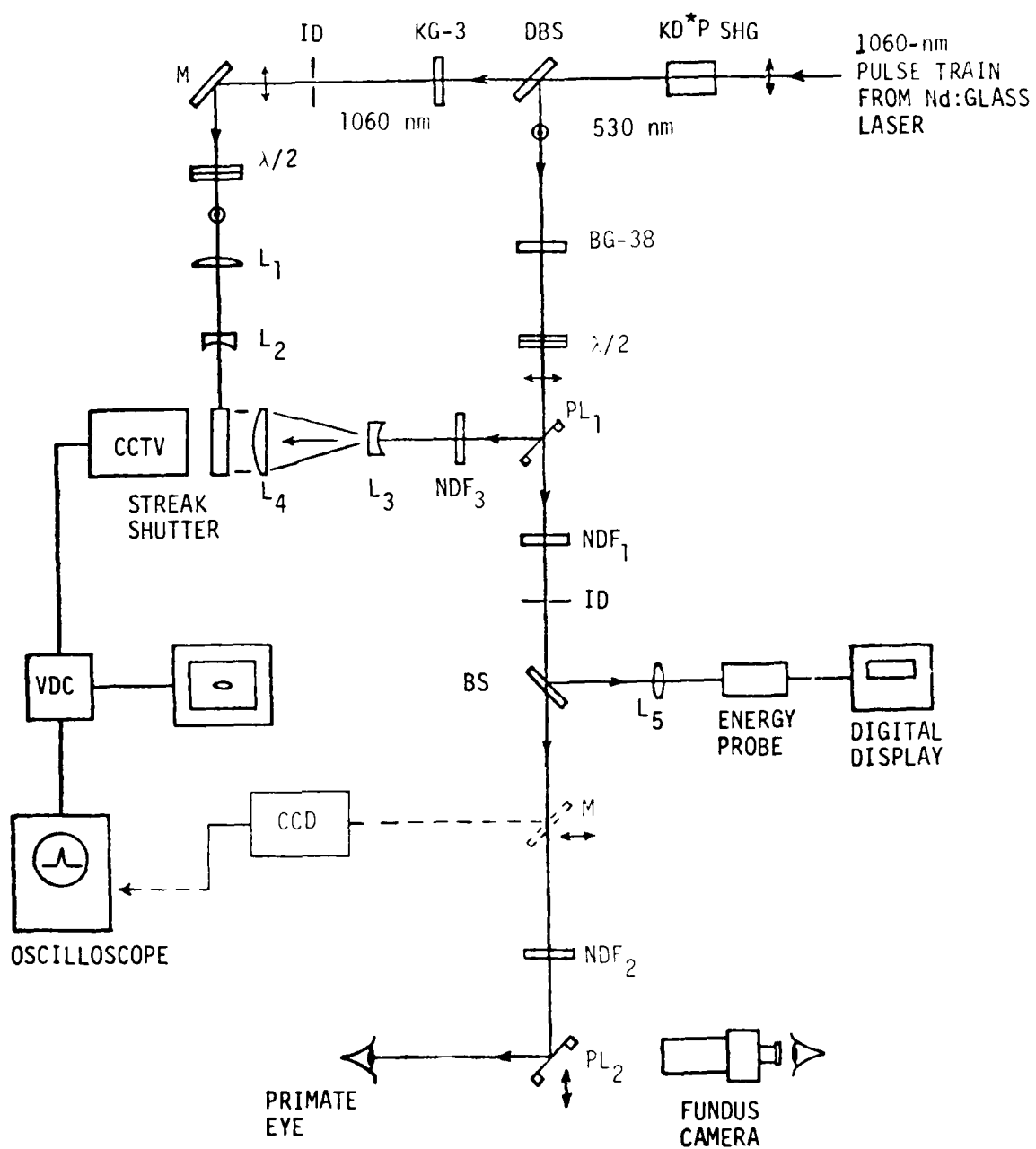


Figure 4. Schematic of apparatus for irradiation of primate eyes with entire trains of ultrashort 2nd harmonic (530 nm) pulses derived from a mode-locked Nd:Glass laser.

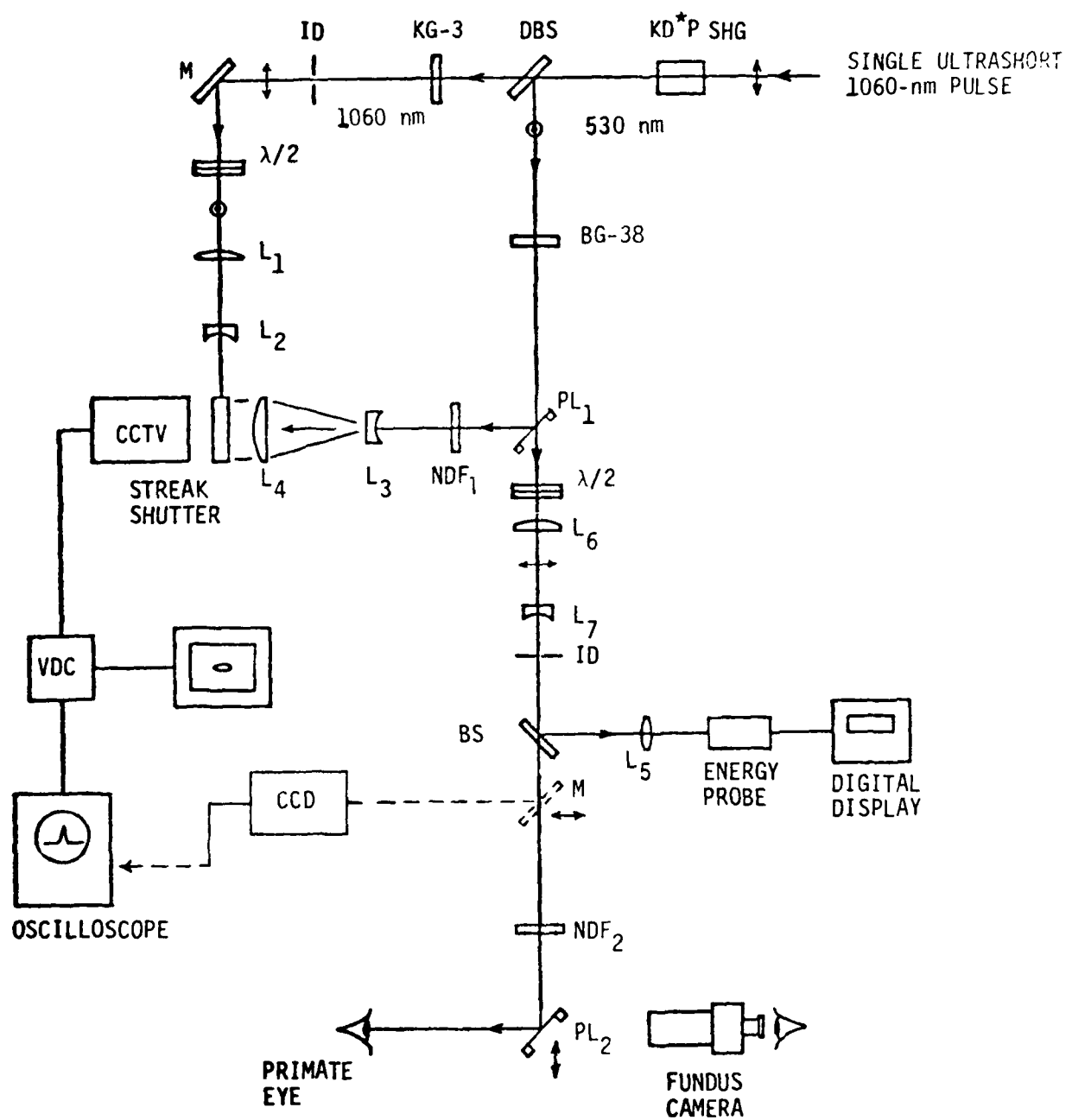


Figure 5. Schematic of apparatus for irradiation of primate eyes with single ultrashort 2nd harmonic (530 nm) pulses derived from a mode-locked Nd:Glass laser.

magnitude since the incident pulse was now vertically polarized. Without this modification not enough light would have entered the pulse chronometer system to yield a detectable signal.

The most significant change made for the single-pulse studies was the addition of a beam-reducing Galilean telescope, comprised of lenses L<sub>6</sub> and L<sub>7</sub>. The diameter of the beam was reduced by a factor of 3.7 so that all of the green pulse energy passed through the 3-mm-aperture iris diaphragm. This beam reduction was necessary so that the single pulses could reliably trigger the pyroelectric energy probe. Without the beam reduction, only about 10% of the pulse energy was transmitted by the aperture, resulting in too low a pulse energy at the energy probe for proper triggering. Unfortunately, the use of the beam-reducing telescope increased the beam divergence by a factor equal to the beam reduction ratio. Thus, the beam divergence, and hence the retinal irradiation spot size, for the single-pulse experiments was 3.7 times greater than in the experiments utilizing the entire pulse train. (The method used to determine the beam divergence is discussed in the section below.) The problem of poor energy probe triggering on single pulses was not discovered until after all of the pulse train data had been obtained, so the two sets of experiments could not be carried out using the same beam divergence.

Control of pulse energy incident on the eye for the single-pulse case was effected by placing calibrated neutral density filters (NDF<sub>2</sub>) between the energy-sampling beamsplitter and the eye to be irradiated. The pulse energy was monitored as described earlier.

Apparatus Common to Both Configurations--The pulse chronometer system, based on a transverse-gated optical Kerr effect shutter, is identical to that used in our macromolecular irradiation studies (Appendix A). It provides an on-line measure of the pulse duration of the IR laser output. The frequency-doubled pulse duration can be deduced from the fact that its intensity scales as the square of IR intensity. Thus, assuming that the laser pulses have a Gaussian temporal shape, the duration of the 530-nm pulse is  $1/\sqrt{2}$  that of the IR pulse. In this work, the IR pulse duration was in the range of 4-13 psec, with an average of 9 psec. It follows that the 530-nm-pulse durations fell in approximately the 3-9-psec range, with an average of ~6 psec.

The beam spatial profiles were measured by directing the 530-nm beam onto a lensless Fairchild CCD camera having 1024 channels/inch. The linear CCD

diode array was placed at the same distance from the iris-diaphragm aperture stop as was the pupil of the test primate. The beam profile was approximately Gaussian in both the single-pulse and entire pulse-train configurations with a  $1/e^2$  diameter of <4 mm at the pupil in each case. Beam divergence was measured in a similar manner, with the CCD array placed at the focal point of a 50-cm-f.l. lens. The divergence was ~6 mrad for the single pulse and ~1.6 mrad for the pulse trains, indicating irradiated spot diameters on the retina of ~78  $\mu\text{m}$  and ~21  $\mu\text{m}$ , respectively, based on a typical value of 1.3 cm for the focal length of the primate eye (53).

The experimental primates were mounted in a prone position on an adjustable platform having 3 degrees of translational freedom ( $x,y,z$ ) and 2 degrees of angular freedom (azimuth and elevation). The pupil of the subject eye could be positioned with respect to the laser beam axis by one or more of these mechanical adjustments. Visual examination of each primate retina was performed for proper placement of the test exposures and for pre- and postexposure examination to determine incurred damage.

A dielectric-coated pellicle beamsplitter ( $\text{PL}_2$ ), attached to a two-position swingaway mount affixed to the fundus camera objective barrel, directed the laser pulse into the eye. In the "down" position the beamsplitter reflected 21.0.5%\* of the incident laser energy into the eye, collinearly with the optic axis of the fundus camera, thus permitting simultaneous observation of the irradiation event. This on-line observation capability permitted precise positioning of the irradiated spot, allowing corrections for eye motion right up to the time the laser was fired. With the beamsplitter in the "up" position, the eye could be examined and photographed with no loss of illumination, or vignetting.

#### Experimental Protocol

Ten Macaca fascicularis primates were used in the experiments. Prior to the irradiation studies the primates were refracted in each eye to

\*The 45° reflection coefficient of the dielectric-coated beamsplitter for horizontally polarized light at 530 nm was determined experimentally, using a collimated CW light source of the correct wavelength and polarization, chopped at a frequency of 330 Hz, and a photomultiplier detector. The reflectivity was deduced from measurements of the transmission factor, using the fact that absorption losses in the coating are less than 0.2%.

determine the corrective lenses required. (Pupil dilation and cycloplegia were obtained by instillation of two drops of Kupfer's solution, a one-to-one mixture of 1% cyclopentolate and 10% phenylephrine.) Any eye with a refractive error greater than 1.50 diopters in any meridian was not used in the experiments.

One day prior to the retinal irradiations of a given primate, pupillary dilation was initiated by instillation of two drops of atropine sulfate (4% solution). This was followed, immediately prior to irradiation, by two drops of Kupfer's solution. Approximately 30 minutes prior to irradiation, each animal was deeply sedated with an intramuscular injection of 0.6 cc ketamine HCl. Booster doses of 0.2 cc ketamine were administered during the course of the experiment as needed. No additional general anesthetics or tranquilizers were required. Eye movements were eliminated by retrobulbar injections of xylocaine (0.35 cc each side of the orbit). A subcutaneous injection of 0.15 cc atropine sulfate served to suppress drooling.

During the exposure procedures the eyelids were kept retracted by a pediatric stainless-steel speculum. Corneal dessication was prevented by frequent irrigation with normal saline, using a modified hypodermic syringe equipped with a 13-G short cannula aimed at the eye. The syringe was connected to the saline solution container through a T-type double ball valve. The syringe acted as a positive displacement manual pump in this configuration and was adjusted to deliver 2 cc of saline per stroke of the spring-loaded plunger.

To guide the placement of the irradiation sites, eight marker lesions, four arranged vertically and four horizontally, were placed adjacent to the macula, as shown in Figure 6. These markers defined a cartesian coordinate system for the 16 test exposures within the macula. (In some cases a fifth row or column was also irradiated for a total of 20 exposure sites within the macula.) The horizontal marker row was always inferior to the macula, whereas the vertical row was temporal in the right eye and nasal in the left eye. The marker lesions were produced with the same laser system used to produce the experimental lesions, but at considerably higher energy. The entire pulse train of 530-nm light was used at an incident energy of 30-50  $\mu$ J. The resulting lesions appeared immediately in most cases and had a diameter ~3 times the spot size of the laser beam at the retina. Most of the marker lesions appeared as whitish discolorations, although a few exhibited some subretinal hemorrhaging, probably a result of damaging hidden capillaries.

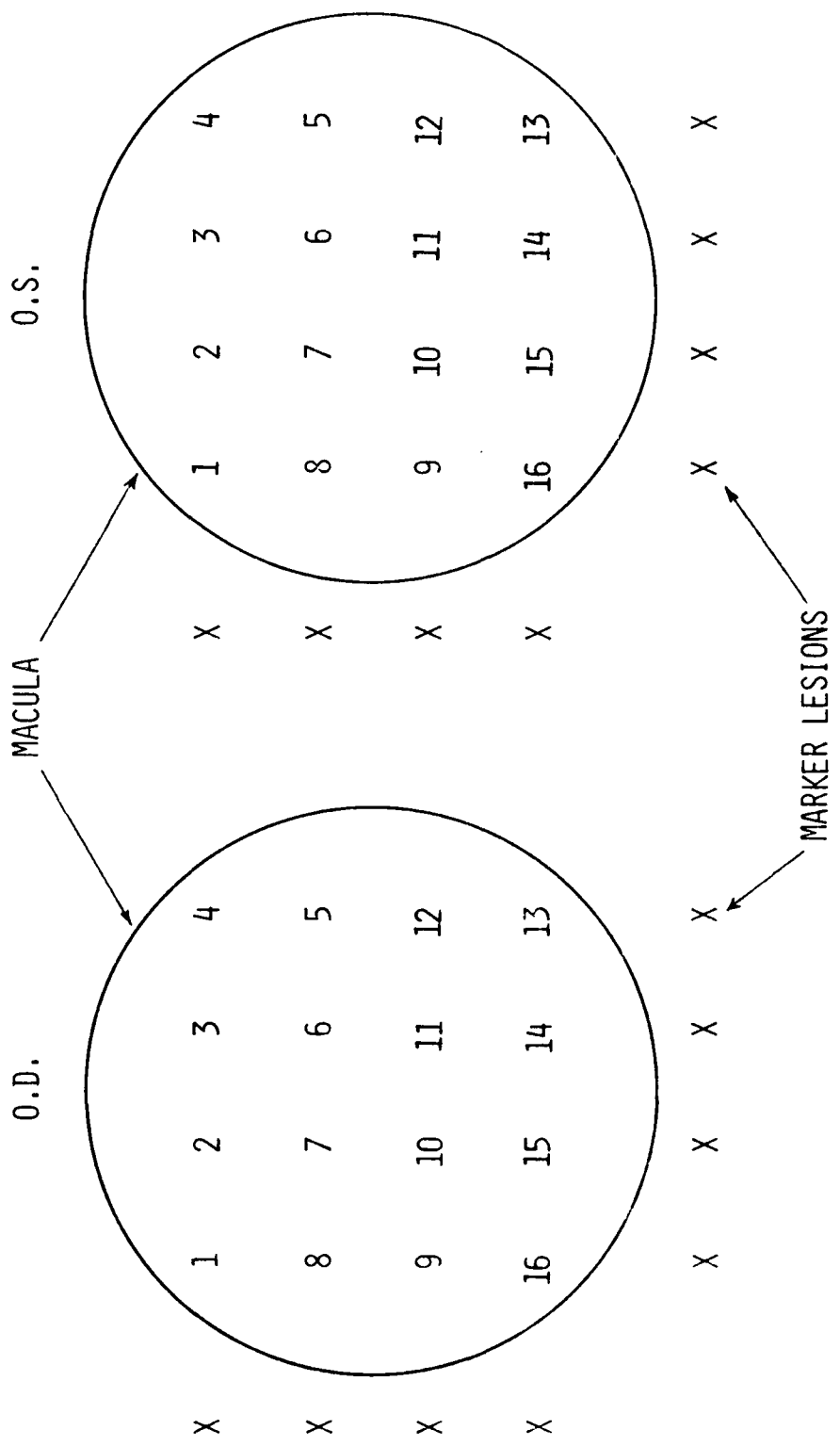


Figure 6. Schematic of macular exposure sites in *M. fascicularis* retina.

Cross-hairs in the eyepiece of the fundus camera were used to align the exposure site with the marker lesions. The animal was moved relative to the laser beam to change the exposure site. The approximate energy range of a given series of exposures was adjusted by the first neutral density filter stack ( $NDF_1$ ). (See Fig. 4.) Final adjustments were made with the calibrated neutral density filters ( $NDF_2$ ). The laser itself provided a degree of randomness in the incident energy as a result of its fluctuations in output from shot to shot. The IR output of the laser typically fluctuates over a range of 25% of its average output. Since the frequency-doubled energy scales as the square of the IR output, the 530-nm incident energy fluctuated over a range of 50% from shot to shot. In cases where a single pulse was selected from the pulse train, the fluctuation was even greater because of the varying efficiency of pulse selection by the Pockels cell from shot to shot. (See Appendix A.) This randomness in the energy delivered to successive exposure sites was useful in preventing bias when evaluating the postexposure sites.

### Results

The maculae of each primate were examined with the fundus camera by two observers for the presence or absence of visible lesions at 1 hour and 24 hours post exposure. A lesion was defined as the smallest observable circular discoloration (usually whitish or light gray) differing from the retinal background. Using this criterion, 148 exposures were made in the range of 0.089-19.5  $\mu$ J with the whole pulse train, and 158 exposures in the range of 0.01-7.1  $\mu$ J with single pulses, to establish the  $ED_{50}$  point (the energy required to produce a lesion in 50% of the events) in each case.

Before the data were analyzed, the pulse-train and pulse-width data were carefully examined to eliminate invalid exposure sites. The criteria for this test were as follows:

(1) For pulse trains, the train had to be clean; i.e., consist of a series of ~100 equally spaced pulses. Interlaced multiple-pulse trains or the presence of spurious pulses between the main pulses were cause for data rejection.

(2) For single pulses, more than 90% of the energy had to be in one pulse. On a number of occasions two successive pulses in the train were switched out by the Pockels cell. Such events were not used in the data reduction.

Occasionally, spurious pulses spaced a few tens of picoseconds from the selected pulse would appear. Those data shots were also rejected.

In addition, exposure data were rejected if during the actual laser shot the laser spot geometry deviated appreciably from a circular geometry or if it appeared fuzzy and significantly larger than normal. (Such effects could be caused by gross refractive errors resulting from distortion of the cornea by the speculum or by side effects of the retrobulbar injections.) Using this criterion alone, all data from three eyes had to be rejected.

In the case of the whole pulse train experiments, 77 exposure events passed the above criteria. With the single-pulse experiments, 108 events passed. These numbers were sufficient to establish reliable  $ED_{50}$  thresholds for each category.

The data were submitted to standard statistical probit analyses (54) to determine the  $ED_{50}$  points (55). The analyses were carried out on all exposure sites in all eyes exposed to a given set of conditions. Implicit in this combined-probit approach is the assumption that the variability from eye to eye is no greater than the variability among sites within a given macula. This assumption has been demonstrated by others to be valid (23). The calculations, however, were carried out separately for the lesion/no-lesion data of each of the two observers. Table 9 presents the 1-hour and 24-hour  $ED_{50}$  points for each observer, with the associated 95% confidence ranges noted in parentheses.

TABLE 9. RETINAL DAMAGE THRESHOLDS AT 530 nm

Pulse train	Single pulse	Evaluation time	Obs. A	Obs. B	Energy density at retina* (Average of both observers)
X		1 hr	4.22 $\mu$ J (3.64-4.91)	4.46 $\mu$ J (3.76-5.29)	1.1
X		24 hr	1.89 $\mu$ J (1.49-2.38)	2.31 $\mu$ J (1.87-2.84)	0.54
	X	1 hr	0.61 $\mu$ J (0.38-0.98)	1.03 $\mu$ J (0.65-1.64)	$1.5 \times 10^{-2}$
X		24 hr	0.24 $\mu$ J (0.17-0.35)	0.24 $\mu$ J (0.15-0.39)	$4.4 \times 10^{-3}$

These data corrected for transmission factor of 0.88 of clear ocular media at 530 nm (29).

The ED<sub>50</sub> thresholds for single-pulse lesions are considerably lower than the thresholds obtained with the entire pulse train. This is especially evident in the 24-hour results in which there is apparently a one-order-of-magnitude difference between the single-pulse and whole pulse-train thresholds. The difference is actually much greater when we consider the fact that the retinal spot size for the single-pulse case ( $\sim 78 \mu\text{m}$ ) is  $\sim 3.7$  times greater than for the pulse-train case ( $\sim 21 \mu\text{m}$ ). Thus the energy density at the retina is an additional factor of 13.7 lower for the single-pulse case. In other words, the actual threshold for damage for the single-pulse case is about two orders of magnitude below that for an entire pulse train, in terms of the energy density deposited at the retina, as is evident in the last column of Table 9.

An interesting deduction that can be made based on our results is that, for the case of the pulse train, the lesion event may actually be caused by the first pulse that reaches the threshold energy for a single pulse. Generally this occurs near the beginning of the train. The reasoning is simple: There are  $\sim 100$  pulses in the train and thus the energy per pulse is  $\sim 1/100$  of the total, which is approximately the same factor by which the single-pulse threshold is smaller than the pulse-train threshold in terms of energy density at the retina. The remaining pulses in the train thus would seem to only add "insult to injury." This also suggests that, if no pulse in the train meets the threshold energy value for single pulses, there may be no damage regardless of the number of pulses in the train, as long as the total pulse-train duration is less than a few microseconds. For longer trains, thermal effects may begin to come into play and this hypothesis would be invalid.

It is instructive to compare the retinal damage thresholds at 530 nm to the results of our earlier vesicle damage studies at 1060 nm, in terms of incident energy density, power density, and corresponding electric-field strength. Table 10 shows that the 24-hr retinal thresholds are remarkably close to the vesicle thresholds for both the pulse train and single pulses, also that the damage threshold for a single pulse is about two orders of magnitude below that for an entire pulse train of 100 pulses for both the vesicles and the retina. This is a strong indication that the damage mechanism in both cases is dependent on the peak power density, and hence the peak electric field in the individual pulse, rather than on the total deposited energy density. The similar results lend credence to the hypothesis forwarded earlier that the

first pulse in the train to reach or exceed the single-pulse threshold will cause the damage. Subsequent pulses in the train would increase the number of damaged vesicles or cells but would not be necessary for a detectable change or lesion.

TABLE 10. COMPARISON OF THRESHOLD DAMAGE DATA FOR VESICLES AND RETINAS

	Vesicle Damage Thresholds (λ = 1060 nm, Δt = 10 psec)			Retinal Damage Thresholds* (λ = 530 nm, Δt = 6 psec)			
	Energy J/cm <sup>2</sup>	Power GW/cm <sup>2</sup>	Peak electric field V/cm × 10 <sup>5</sup>		Energy J/cm <sup>2</sup>	Power GW/cm <sup>2</sup>	Peak electric field V/cm × 10 <sup>5</sup>
Pulse train	0.6	0.6	5.8	1 hr 24 hr	1.1 0.54	1.8 0.90	10 7.1
Single pulse	9×10 <sup>-3</sup>	0.9	7.1	1 hr 24 hr	1.5×10 <sup>-2</sup> 4.4×10 <sup>-3</sup>	2.5 0.73	13 6.4

\*Retinal damage thresholds are corrected for the transmission factor of the clear ocular media at 530 nm.  $T_{530} = 0.88$  (29).

Since the electric fields associated with the threshold values are nearly an order of magnitude greater than the membrane potentials of both the vesicle and cell lipid bilayer membranes, it appears reasonable at this time to ascribe the ocular damage to membrane disruption by electrostrictive forces.

This tentative identification of the damage mechanism must be tempered somewhat, at least at present, by a number of factors. First, the wavelengths used in the vesicle and retinal work are not the same. Thus, photobiological processes may be present in the retinal case and the damage may not be a result of membrane disruption by electric fields. Unfortunately, it was not possible to generate sufficient power in the 2nd harmonic of the Nd:Glass laser to attain the 1060-nm threshold levels for the vesicles at 530 nm. Such an experiment would require a laser amplifier of gain 3, which was not available to us at the time of the research. Thus, the wavelength dependence of vesicle damage could not be determined.

Second, the vesicle data are based on relatively few individual experiments, so their damage threshold determination is statistically less reliable than for the retinae. The reason for the relatively few data points is that the preparation of the vesicle samples, their irradiation, and their subse-

examination by dynamic light scattering are very time consuming. No more than one or two samples a week could be studied in this manner, whereas all of the retinal data (320 data points) were gathered in a matter of a few weeks.

Finally, the vesicles we studied were not subject to osmotic pressure imbalances or chemical potential gradients across the membrane, whereas such effects are present in living cells. In the living cell the disruption of the membrane by the electric field in a single threshold laser pulse would be facilitated by the osmotic pressure imbalance across the membrane, resulting in irreversible damage.

#### Comparison with Other Work

The 24-hr postexposure results reported here are compared in Table 11 with the results of similar experiments carried out by Ham et al. at 1064 nm (28), Goldman et al. at both 532 nm and 1064 nm (29), and Taboada et al. at 1060 nm (30,31). A considerable discrepancy appears not only in the ED<sub>50</sub> values but also in the threshold power density and electric field at the retina. In addition to differences in wavelength and pulse duration, a number of possible factors related to experimental protocol and the definition of a threshold lesion can significantly affect the experimental results.

One factor may be that in none of the work is the diameter of the irradiated spot size at the retina known with a great degree of certainty. This is a difficult parameter to measure *in vivo* (the diameter of the lesion is not necessarily the same as that of the irradiated spot); consequently, the spot size is usually estimated from a knowledge of the laser beam divergence and an estimate of the effective focal length of the emmetropic primate eye.

Although all researchers, including ourselves, have used corrective lenses if the refractive error of the primate eye exceeded  $\pm 0.5$  diopter in any plane, nonintrinsic refractive errors can arise during the irradiation experiments. On a number of occasions, for example, we have observed otherwise normal eyes become highly astigmatic during an experiment, possibly as a result of delayed adverse reaction to the retrobulbar injections or, to a lesser extent, in response to the forces exerted by the eyelid retracting speculum.

On other occasions we also noted that the visibility of the retina through the fundus camera was greatly reduced due to opacification of the

TABLE 11. COMPARISON OF PRESENT RETINAL THRESHOLDS WITH RESULTS  
OF OTHER INVESTIGATIONS (24 HR POST EXPOSURE)

Work	Wavelength (nm)	Type of pulse	Pulse duration (psec)	ED <sub>50</sub> at cornea (μJ)	Irradiated spot diameter (μm)	Conditions at Retina <sup>a</sup>		
						Energy (J/cm <sup>2</sup> )	Power (GW/cm <sup>2</sup> )	Electric field (V/cm×10 <sup>5</sup> )
Present	530	train (100 pulses)	6	2.1	21	0.54	0.9	7.1
Present	530	single	6	0.24	78	4.4×10 <sup>-3</sup>	0.73	6.4
Hann et al. (28)	1064	single	30	13	25	2.0	67	60
Goldman et al. (29)	1064	single	30	8.7	25	1.3	90	70
Goldman et al. (29)	530	single	30	18.2	25	2.8	22	34
Taboada et al. (30)	1060	train (13 pulses)	6	0.017	50	6.6×10 <sup>-4</sup>	0.11	2.5
Taboada et al. (31)	1060	single	6	2.2	30	0.24	40	46

cornea. Frequent irrigation with normal saline did not always improve visibility.

The above factors can lead to considerable error in the estimation of the irradiated spot size and to significant attenuation of the incident beam due to corneal scattering. In either case, the radiant exposure at the retina could be significantly lower than expected, resulting in high values of ED<sub>50</sub>.

The experiments reported here are the only ones in the picosecond regime in which the fundus was observed during actual firing of the laser. The laser was fired only under conditions of maximum clarity of the ocular media. If any gross astigmatism was evident at any time during an experiment, the data for that eye were rejected. Not all previous work has followed such precautions.

Other variances in exposure protocol and, particularly, variances in threshold determination can also significantly affect the experimental results. In two cases (28,29) the definition of a threshold lesion was one which became just visible fundoscopically within 24 hr of exposure. No statistical analyses of the data were undertaken by those workers, so the determination of what constituted a threshold lesion was very sensitive to the observer's subjective interpretation. On the other hand, the work of Taboada et al. (30,31) and the results presented here made use of probit analysis to determine the damage thresholds and are thus less prone to subjective errors.

#### CORNEAL DAMAGE THRESHOLDS INDUCED BY PICOSECOND 265-nm LIGHT PULSES

##### Irradiation Apparatus

The facility used in the UV corneal irradiation experiments was in most respects similar to that used in the 530-nm retinal exposure experiments. A schematic of the apparatus is shown in Figure 7. When compared with the facility shown in Figure 4, the UV facility differed in two respects: (1) a temperature phase-matched KD\*P crystal was added to frequency-double the 530-nm light to 265 nm; (2) the primate was placed so that the UV beam impinged on the cornea directly, without deflection by a beamsplitter or mirror.

In addition, a pair of Schott UG-5 UV bandpass filters, having a combined transmission of 50% at 265 nm and <10<sup>-6</sup> at 530 nm, was placed at the output of the 4th harmonic crystal to eliminate the 530-nm light. A 20-cm-f.l. fused

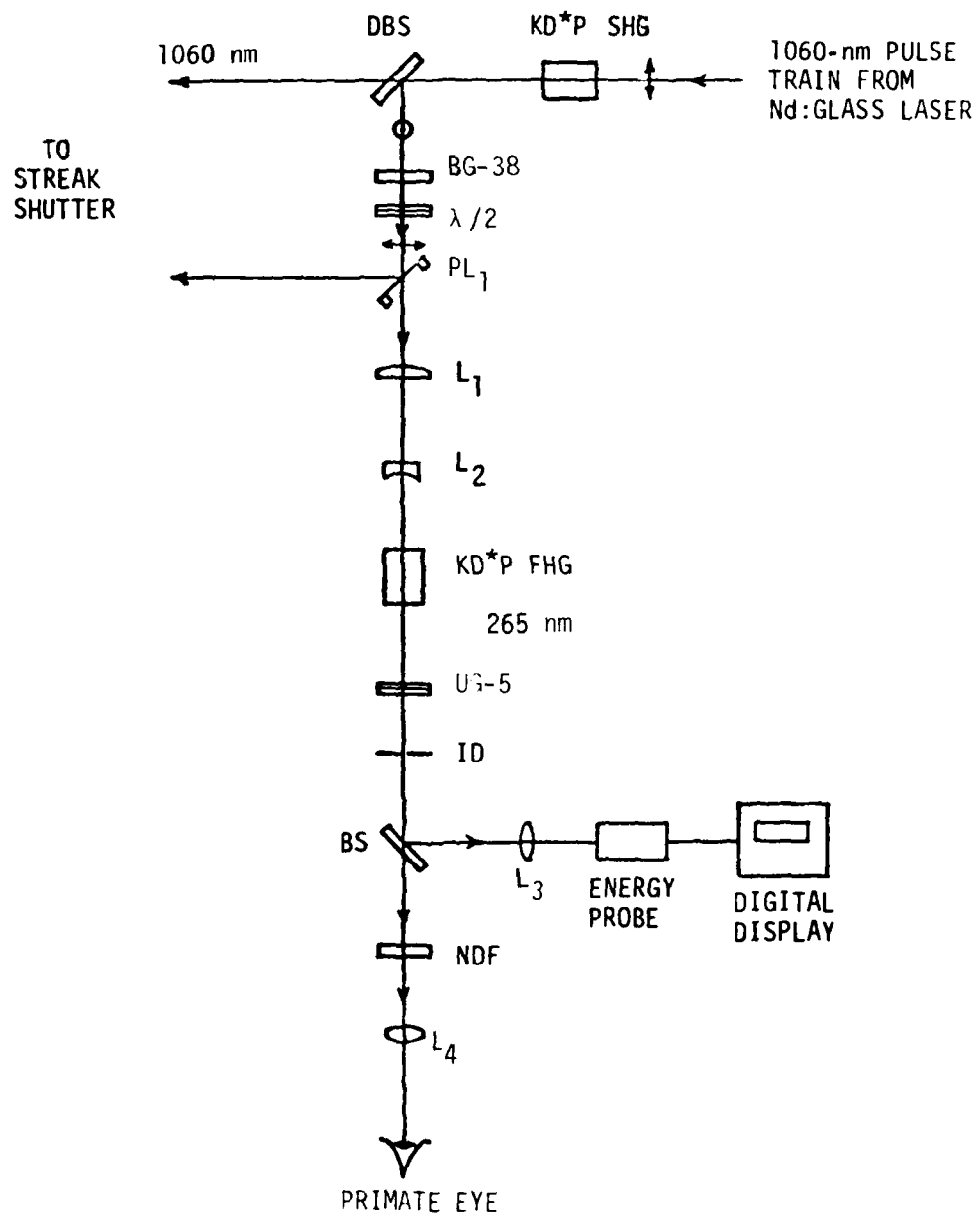


Figure 7. Schematic of apparatus for irradiation of primate eyes with ultrashort 4th harmonic (265 nm) pulse trains derived from a mode-locked Nd:Glass laser.

quartz (Suprasil) lens ( $L_4$ ) was used to vary the beam diameter impinging on the cornea to vary the incident intensity over the desired range. A set of calibrated UV neutral density filters (NDF) was used for additional control of intensity. All neutral filters ahead of the UV generator were removed to assure maximum conversion efficiency. In this same regard, the beam diameter of the 530-nm light was reduced by a factor of 3.7 by lens pair  $L_1 - L_2$  to increase the intensity and thus the UV conversion efficiency in the FHG crystal. The aperture stop was set at 3 mm as in the case of the 530-nm experiments.

The beam diameter at the cornea was set by varying the distance between the cornea and the focusing lens ( $L_4$ ). Maximum diameter was obtained by removing the lens. The cornea-to-lens separations used in the experiments were 10, 15, and 20 cm. Other values of incident energy density were obtained by means of the calibrated UV neutral density filters. The actual beam spot size at the cornea was determined by a fluorescence technique. At the various locations of the cornea relative to the focusing lens, a strip of Scotch "Magic" transparent tape coated with an ethanolic solution of coumarin dye (Eastman X5419) was placed perpendicular to the UV beam. The very thin coating of dye left on the tape where the alcohol evaporated, fluoresced strongly without any blooming. A closed-circuit TV camera was focused on the rear surface of the tape to record the fluorescent spot. The intensity distribution in this spot was determined by the same video analyzing system used to measure pulse widths with the optical Kerr shutter. Care was taken to eliminate any stray visible or IR light and to assure that the fluorescence response was linear, the latter verified by means of UV neutral density filters. The spot intensity profiles determined in this manner closely followed the Gaussian profile with  $1/e^2$  diameters of 2.9, 1.6, 1.1, and 0.76 mm, corresponding to no lens, and distances of 10, 15, and 20 cm from the focusing lens. These beam sizes were used to calculate the incident energy densities at the irradiated sites.

Pulse duration measurements were carried out as described in Appendix A. Since the 4th harmonic generation scales closely as the fourth power of the laser output, the UV pulse durations are half the pulse durations of the 1060-nm fundamental. Thus, in this set of experiments, the average duration of each pulse in the UV pulse train was  $\sim 4.5$  psec.

### Experimental Protocol

The same ten primates (Macaca fascicularis) used in the 530-nm retinal irradiation experiments were used in the UV corneal irradiation experiments. Prior to exposure each primate was prepared as described previously for the 530-nm exposures, with the exception that retrobulbar injections were not necessary here. The corneas of each animal were examined with a hand-held ophthalmoscope prior to the exposure experiment to locate any preexisting corneal lesions. Only one eye had a preexisting lesion and its character was recognizably different from laser-induced lesions. Four sites were exposed on each cornea, as shown in Figure 8. Only entire pulse trains were used in this study, due to the relatively low UV energy available; the single-pulse energy was too low to trigger the energy probe reliably. A total of 80 sites were exposed over an incident energy density range of 1.3 to 70 mJ/cm<sup>2</sup>, using the method described in the Irradiation Apparatus section to vary the energy density.

### Results and Discussion

The corneas were carefully examined with an ophthalmoscope immediately after exposure, 1 hr post exposure, and 24 hr post exposure. In addition, at 24 hr post exposure, the corneas were examined with a Nikon slit-lamp biomicroscope. This examination was done both in white light and with cobalt blue light. In the latter case, sodium fluorescein dye was introduced into the eye by the standard technique of inserting a dye-impregnated paper strip under the lower eyelid and then spreading the released dye over the cornea by blinking the eyelids manually. The sodium fluorescein adheres preferentially to the corneal lesions and glows greenish yellow under cobalt blue illumination. This was the most sensitive test for the existence of threshold lesions. The results were recorded photographically as well as visually. No lesions were detected either immediately or 1 hr post exposure, even at the highest energy densities. However, epithelial lesions were observed in about half the cases at 24 hr post exposure. Under white-light illumination, the lesions appeared as small circular grainy opacifications, having a diameter somewhat smaller than the UV beam diameter. None of the lesions appeared to have any significant depth. Stained with sodium fluorescein and observed under cobalt

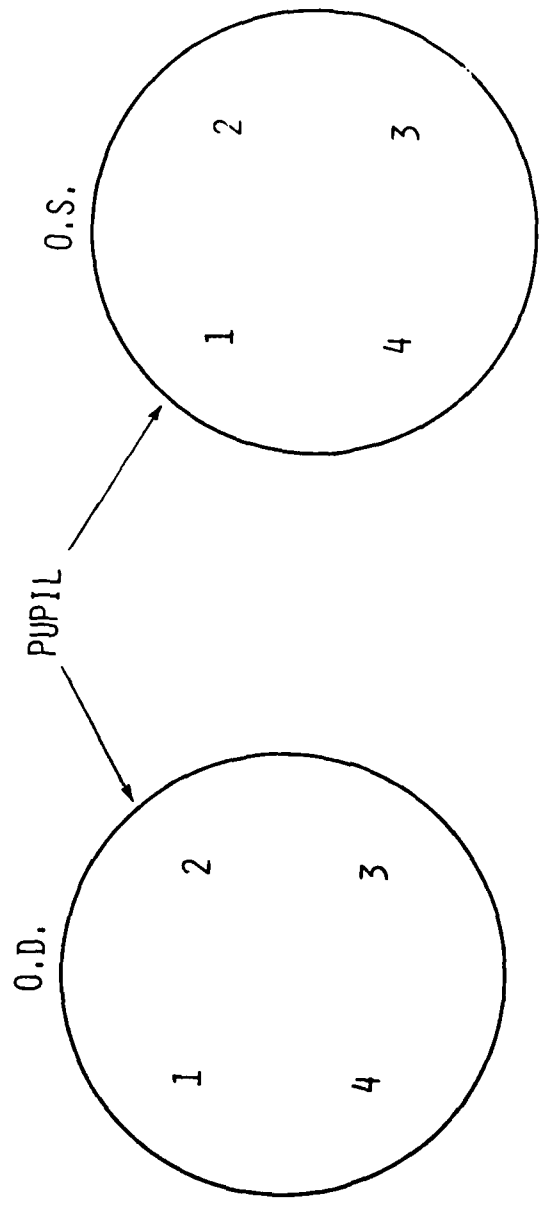


Figure 8. Schematic of exposure sites on *M. fascicularis* cornea.

blue illumination, the lesions stood out more clearly. In all cases the lesion/no-lesion events were recorded by two observers.

The lenses of eyes that exhibited corneal lesions were also examined with the slit-lamp for the possible presence of UV-induced cataracts. However, unlike work reported at longer wavelengths, >325 nm (26,27), no signs of any lenticular opacification were seen in any of the eyes. Retinal examinations were not made since the subject animals had been previously used in the 530-nm retinal damage studies.

The data were statistically analyzed using the method of probits, as for the 530-nm retinal exposures. An ED<sub>50</sub> threshold was definable only 24 hr post exposure, as no lesions were observed 1 hr post exposure. Again, only data that represented well-defined operation of the laser were used in the analysis. (A total of 61 events were usable.) The mean of observer values averaged over the eyes gave the following estimate with the associated 95% confidence limits: ED<sub>50</sub> = 8.2 mJ/cm<sup>2</sup> (6.3 - 10.7) at 24 hr post exposure. The corresponding peak power per pulse in the train at the cornea was 18 MW/cm<sup>2</sup>, and the electric field per pulse was ~10<sup>5</sup> V/cm.

There are no data on UV laser effects to which these results can be compared directly. The shortest UV laser wavelength previously studied for corneal damage effects was 337 nm from a pulsed nitrogen laser producing 10-nsec pulse durations (27). In that work the damage threshold was 8.7 J/cm<sup>2</sup>, or three orders of magnitude higher than the present value. No correlations can be made with that result because of the vastly different pulse durations and because corneal tissue, as all biological tissue, exhibits a considerable variation in its adsorption spectrum in the region between 200 nm and 400 nm (2,3).

The only data available at a wavelength close to the 265 nm studied here are those of Pitts et al. (25) at 270 nm for a noncoherent UV source (an arc monochromator) and essentially CW exposure. Pitts and his coworkers found that the peak sensitivity of the cornea to UV photokeratitis was at 270 nm for both the primate and human eye, and they determined the threshold to be 4 mJ/cm<sup>2</sup> for both subjects. This value is comparable in magnitude to our results at 265 nm; however, except for some punctate staining, the experiments of Pitts did not produce well-defined corneal opacities similar to ours.

The primary damage mechanism for picosecond pulses at 265 nm is somewhat speculative at this time, but it appears to be photochemical in nature. Neither the power density nor electric field per pulse in the mode-locked pulse train appears to be sufficient for nonlinear or direct electric-field effects. For example, the peak electric field of  $\sim 10^5$  V/cm carried by the individual pulses is too close in magnitude to the electric field within the cell membranes ( $0.6 \times 10^5$  V/cm) to have a significant effect.

Although the mechanism of the effect of UV radiation on biological systems is only generally understood, we believe that the most likely damage mechanisms at 265 nm are the photochemical alteration, such as denaturation and coagulation, of proteins and nucleic acids. Especially vulnerable are unconjugated nucleoproteins of the cell and the DNA in the chromosomes. Both are particularly susceptible, with maximum sensitivity at 265 nm, since this wavelength lies at or near the center of their action spectra (2,3). Further work needs to be carried out at 265 nm in a manner similar to our experiments in the visible and near IR to confirm this damage mechanism.

## REFERENCES

1. Sliney, D.H. The development of laser safety criteria--biological considerations. In M.R. Wolbarsht (ed.). *Laser applications in medicine and biology*, Vol. I. New York: Plenum Press, 1971.
2. Michaelson, S.M. Human exposure to nonionizing radiant energy--potential hazards and safety standards. *Proc IEEE* 60:389 (1972).
3. Sliney, D.H., and B.C. Freasier. Evaluation of optical radiation hazards. *Appl Opt* 12:1 (1973).
4. Goldman, L., D.W. Fradin, N. Bloembergen, and D.F. Richfield. Studies in laser safety of new high-output systems. 1. Picosecond impacts. *Opt Laser Tech* 5:11 (1973).
5. Goldman, L., E. Yablonovitch, N. Bloembergen, and D. Richfield. Studies in laser safety of new high-output systems. 2. TEA CO<sub>2</sub> laser impacts. *Opt Laser Tech* 5:58 (1973).
6. Mainster, M.A., T.J. White, and R.G. Allen. Spectral dependence of retinal damage produced by intense light sources. *J Opt Soc Am* 60:848 (1970).
7. Sliney, D.H., et al. Laser hazards bibliography. U.S. Army Environmental Hygiene Agency, Aberdeen Proving Ground, Md., May 1975.
8. Dunsky, I.L., and P.W. Lappin. Evaluation of retinal thresholds for CW laser radiation. *Vision Res* 11:733 (1971).
9. Bresnick, G.H., et al. Ocular effects of argon laser radiation. *Invest Ophthalmol* 9:901 (1970).
10. Ham, W.T., et al. Helium-neon laser in the rhesus monkey. *Arch Ophthalmol* 84:798 (1970).
11. Frisch, G.D., E.S. Beatrice, and R.C. Holsen. Comparative study of the argon and ruby retinal damage thresholds. *Invest Ophthalmol* 10:911 (1971).
12. Vassiliadis, A., H.C. Zweng, N.A. Peppers, and R.R. Peabody. Thresholds of laser eye hazards. *Arch Env Health* 20:161 (1970).
13. Ebbers, R.W. Retinal effects from multiple-pulse gallium arsenide lasers. SAM-TR-72-25, Nov 1972.
14. Hayes, J.R., and M.I. Wolbarsht. Thermal model for retinal damage induced by pulsed lasers. *Aerosp Med* 39:474 (1968).

15. Lappin, P.W., and P.S. Coogan. Relative sensitivity of various areas of the retina to laser radiation. *Arch Ophthalmol* 84:350 (1970).
16. Gibbons, W.D., and D.E. Egbert. Ocular damage thresholds for repetitive-pulse laser exposures. *SAM-TR-74-1*, Feb 1974.
17. King, R.G., and W.J. Geeraets. The effect of Q-switched ruby laser on retinal pigment epithelium in vitro. *Acta Ophthalmol* 46:617 (1968).
18. Ebbers, R.W., and I.L. Dunsky. Retinal damage thresholds for multiple-pulse lasers. *Aerospace Med* 44:317 (1973).
19. Adams, D.O., D.J. Lund, and P.D. Shawaluk. The nature of chorioretinal lesions produced by the gallium arsenide laser. *Invest Ophthalmol* 13:471 (1974).
20. Gibson, G.L.M. Retinal damage from repeated subthreshold exposures using a ruby laser photocoagulator. *SAM-TR-70-59*, Oct 1970.
21. Gibbons, W.D., and R.G. Allen. Evaluation of retinal damage produced by long-term exposure to laser radiation. *SAM-TR-75-11*, Apr 1975.
22. Gibbons, W.D. Retinal burn thresholds for exposure to a frequency-doubled neodymium laser. *SAM-TR-73-45*, Nov 1973.
23. Hemstreet, H.W., Jr., J.S. Connolly, and D.E. Egbert. Ocular hazards of picosecond and repetitive-pulse lasers. Vol. I: Nd:YAG laser (1064 nm). *SAM-TR-78-20*, Apr 1978.
24. Cleary, S.F., and P.E. Hamrick. Laser-induced acoustic transients in the mammalian eye. *J Acoust Soc Am* 46:1037 (1969).
25. Pitts, D.G., and T.J. Tredici. The effects of ultraviolet radiation on the eye. *Am Indust Hyg Assoc J* 32:235 (1971).
26. Ebbers, R.W., and D. Sears. Ocular effects of a 325-nm ultraviolet laser. *Am J Optom Physiol Opt* 52:216 (1975).
27. Zuchlich, J.A., and J.S. Connolly. Ocular damage induced by near-ultraviolet laser radiation. *Invest Ophthalmol* 15:760 (1976).
28. Ham, W.T., Jr., H.A. Mueller, A.I. Goldman, B.E. Newman, L.M. Holland, and T. Kuwabara. Ocular hazard from picosecond pulses of Nd:YAG laser radiation. *Science* 185:362 (1974).
29. Goldman, A.I., W.T. Ham, Jr., and H.A. Mueller. Ocular damage thresholds and mechanisms for ultrashort pulses of both visible and infrared laser radiation in the rhesus monkey. *Exp Eye Res* 24:45 (1977).
30. Taboada, J., and R.W. Ebbers. Ocular tissue damage due to ultrashort 1060-nm light pulses from a mode-locked Nd:glass laser. *Appl Opt* 14:1759 (1975).

31. Taboada, J., and W.D. Gibbons. Retinal tissue damage induced by single ultrashort 1060-nm laser light pulses. *Appl Opt* 17:2871 (1978).
32. Boettner, E.A., and J.R. Wolter. Transmission of the ocular media. *Invest Ophthalmol* 1:776 (1962).
33. Bruckner, A.P., J.M. Schurr, N.B. Martin, and E.L. Chang. Observation of changes induced by picosecond light pulses in suspensions of dipalmitoyl phosphatidyl choline vesicles. *Appl Opt* 18:1876 (1979).
34. Bruckner, A.P., J.M. Schurr, and E.L. Chang. Ultrashort laser pulse induced electromagnetic stress on biological macromolecular systems. SAM-TR-79-3, Nov 1979.
35. Thomas, J.C., S.A. Allison, J.M. Schurr, and R.D. Holder. Dynamic light scattering studies of internal motions in DNA. II. Clean viral DNA's. *Biopolymers* 19:1451 (1980).
36. Bloomfield, V.A., D.M. Crothers, and I. Tinoco, Jr. Physical chemistry of nucleic acids. New York: Harper and Row, 1974.
37. Lin, S.C., J.C. Thomas, S.A. Allison, and J.M. Schurr. Dynamic light scattering studies of internal motions in DNA. III. Evidence for titratable joints associated with bound polycations. *Biopolymers* 20:209 (1981).
38. Fangman, W. Separation of very large DNA molecules by gel electrophoresis. *Nucleic Acids Res* 5:653 (1978).
39. Letokhov, V.S. On the possibility of selective biochemical reactions induced by laser radiation. *J Photochem* 4:185 (1975).
40. Oref, I., and B.S. Rabinovitch. Do highly excited reactive polyatomic molecules behave ergodically? *Acct Chem Res* 12:166 (1979).
41. Jackson, J.D. Classical electrodynamics. New York: John Wiley and Sons, Inc., 1962.
42. Kubo, R. Statistical mechanical theory of irreversible processes. I. General theory and simple applications to magnetic and conduction problems. *J Phys Soc Japan* 12:570 (1957).
43. Mathews, J., and R.L. Walker. Mathematical methods of physics. New York: W.A. Benjamin, Inc., 1965.
44. Duguay, M.A., and J.W. Hansen. An ultrafast light gate. *Appl Phys Lett* 15:192 (1969).
45. Debye, P. Polar molecules. New York: Dover Publications, Inc., 1929.
46. Bruckner, A.P. Some applications of picosecond optical range gating. *Proc SPIE* 94:41 (1976).

47. Harrington, R.E. Opticohydrodynamic properties of high molecular weight DNA. III. The effects of NaCl concentration. *Biopolymers* 17:919 (1978).
48. Voordouw, G., Z. Kam, N. Borochov, and H. Eisenberg. Isolation and physical studies of the intact supercoiled, the open circular, and the linear forms of col E<sub>1</sub> plasmid DNA. *Biopolymers* 8:171 (1978).
49. Thomas, J.C., S.A. Allison, C.J. Appelof, and J.M. Schurr. Torsion dynamics and depolarization of fluorescence of linear macromolecules. II. Fluorescence polarization anisotropy measurements on a clean viral φ29 DNA. *Biophysical Chemistry* 12:177 (1980).
50. Kremer, J.M.H., M.W.J. v.d. Esker, C. Pathmamanoharan, and P.H. Wiersma. Vesicles of variable diameter prepared by a modified injection method. *Biochemistry* 16:3932 (1977).
51. Barenholz, Y., D. Gibbes, B.J. Litman, J. Goll, T.E. Thompson, and F.D. Carlson. A simple method for the preparation of homogeneous phospholipid vesicles. *Biochemistry* 16:2806 (1977).
52. Schurr, J.M. Dynamic light scattering of biopolymers and biocolloids. *CRC Critical Reviews of Biochemistry* 4:371 (1977).
53. Harris, C. Personal communication. Center for Bioengineering, University of Washington, 1979.
54. Finney, D.J. Probit analysis, 2nd ed. New York: Cambridge University Press, 1952.
55. Taboada, J. Personal communication. The standard probit statistical analysis of the ocular damage data was conducted in the Laser Effects Branch, USAF School of Aerospace Medicine, Brooks AFB, Tex., Jan 1980.
56. Shimizu, K., A. Ishimaru, L.O. Reynolds, and A.P. Bruckner. Backscattering of a picosecond pulse from densely distributed scatterers. *Appl Opt* 18:3484 (1979).
57. Bruckner, A.P. Picosecond light scattering measurements of cataract microstructure. *Appl Opt* 17:3177 (1978).
58. Chen, S.H., W.B. Veldkamp, and C.C. Lai. Simple digital clipped correlator for photon correlation spectroscopy. *Rev Sci Instrum* 46:1356 (1975).

## APPENDIX A

### PICOSECOND LASER IRRADIATION FACILITY

The ultrashort-pulse laser facility assembled for the purpose of irradiating selected macromolecular samples and primate eyes is illustrated in Figure A-1. It consists of four subsystems: a mode-locked Nd:Glass laser, a high-speed Pockels cell pulse-switching system, a pulse chronometer and video detection system, and a pulse-energy measurement system. Each of these is described below.

#### Nd:Glass Laser

The mode-locked Nd:Glass laser consists of a water-cooled, Brewster-angled, Owens-Illinois ED-2 glass rod, 1.3-cm dia x 22.9-cm length, pumped by two EG&G linear flashlamps in a double elliptical reflector cavity. The resonator is formed by a flat 99.7% rear reflector ( $M_1$ ) and a 10-m radius 35% output reflector ( $M_2$ ). Mode-locking is accomplished by a flowing 1-mm-thick dye cell placed in direct contact with the rear reflector. The dye solution consists of Eastman 9860 dye in dichloroethane at a concentration that results in a small-signal transmission factor of ~60% at 1060 nm. An iris diaphragm ( $ID_1$ ) is used to control transverse mode size and purity. By closing it down to an aperture of 5-mm dia or less,  $TEM_{00}$  output can be obtained. In the above configuration the laser produces a train of ~100 horizontally polarized pulses at  $\lambda = 1060$  nm, each of  $\leq 10$ -psec duration and  $>100$ -MW peak power, spaced at 5.6-nsec intervals (the round-trip cavity time).

The choice of dye cell geometry is critical to laser performance. We have experimented with various types of discrete dye cells and with the contacted type, with and without dye circulation, and have found that the circulating contacted cell produces the most consistent and reproducible pulse trains, with excellent suppression of satellite pulses. Beam stability and mode purity are also optimized with this configuration.

At one point in the program we experienced difficulties in proper mode-locking of our glass laser on account of the poor quality laser-grade

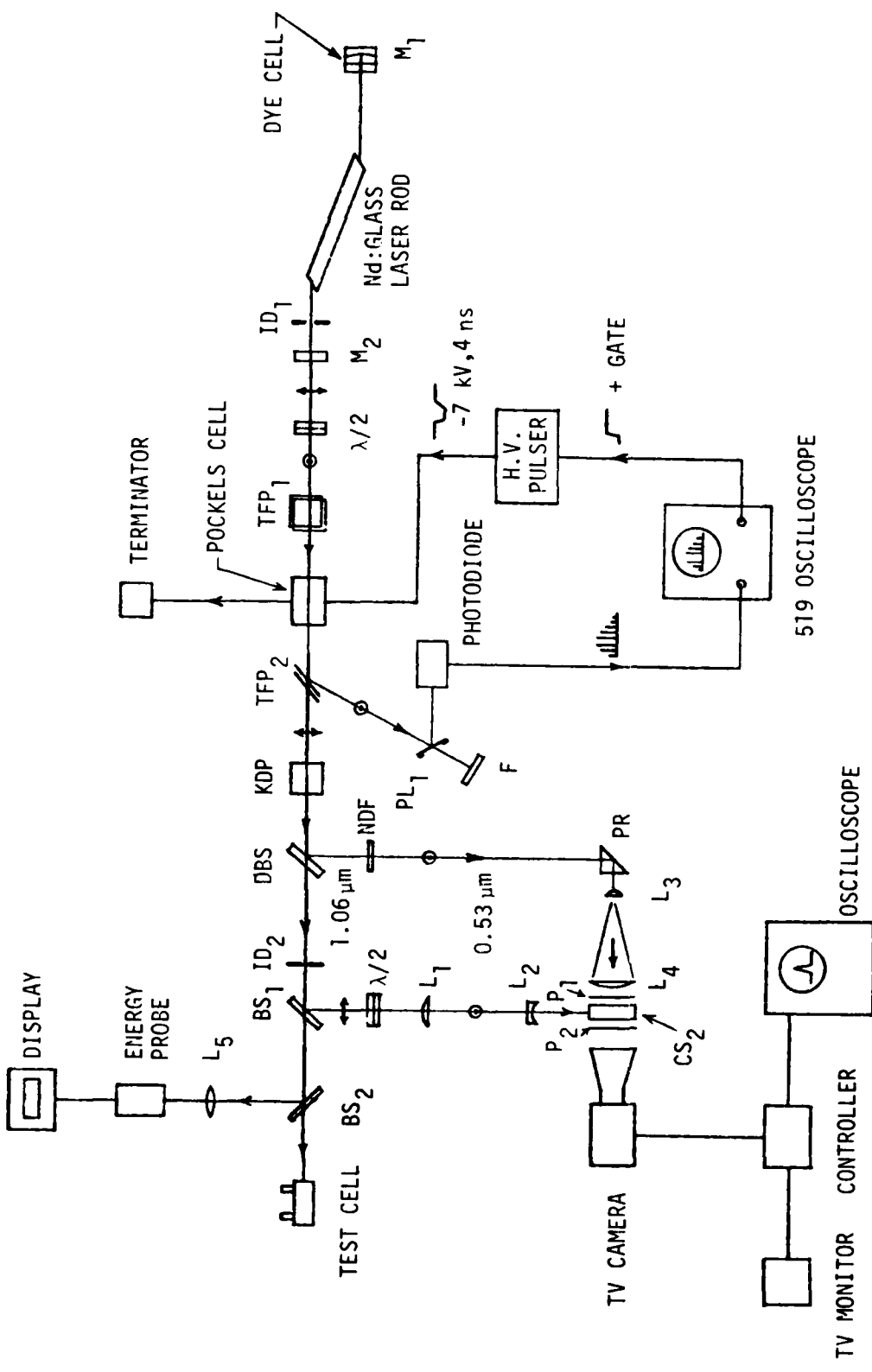


Figure A-1. Schematic of apparatus for picosecond laser irradiation of macromolecular systems.

1,2 dichloroethane supplied by Eastman Organic Chemicals. Apparently, high quantities of residual HCl were present in their then-available lot, No. A6B, which destroyed the 9860 saturable dye immediately upon mixing. No mode-locking at all was obtained using this particular lot of solvent. A search through various chemical distributors turned up some dichloroethane of a different lot number (A4C), which worked marginally. The dye solution mode-locked the laser successfully for two or three consecutive days, but then it degraded and had to be replaced.

Because of these difficulties, for some of the experiments the glass laser was mode-locked by Eastman 9740 dye in chlorobenzene instead of the usual 9860 dye in dichloroethane. With the 9740 dye the laser produced the same average total energy per pulse train, but the number of pulses in a train was at most only ~30-50 compared to the average ~80-100 obtained with 9860 dye. Operation of the laser was much more erratic with 9740 than with 9860. Multiple and spurious pulsing occurred on at least half of all mode-locked shots. Only one in three or four firings of the laser resulted in mode-locking at all. Furthermore, due to the higher peak power obtained with 9740 dye, some of the optical components sustained some surface or bulk damage. Because of these difficulties, the use of 9740 dye was discontinued.

The problem of impure dichloroethane was finally solved by filtering the solvent through a 4" column of basic alumina powder, following the suggestion of W. Robinson at Texas Tech University. The purified solvent was then filtered free of residual alumina particles by means of a  $0.45\text{-}\mu\text{m}$  Millipore filter. The entire purification process is slow but very effective. Excellent mode-locking has been achieved using the purified dichloroethane as the solvent for the 9860 dye. Only half the usual concentration of dye is required, and the solution remains stable for weeks at a time. Mode-locking reproducibility has improved considerably also. Spurious or multiple pulsing occurs no more than once in 20-30 shots. Although power output is somewhat lower than in the past ( $150\text{-}200\text{ MW/cm}^2$  compared to  $200\text{-}300\text{ MW/cm}^2$ ), the pulse duration is less. Pulses at the beginning of the pulse train have been measured to have durations in the 6-10-psec range, whereas previously they were in the 10-15-psec range.

### Pockels Cell Pulse-Switching System

To permit irradiating the macromolecular samples or primate eyes with single ultrashort pulses as well as with entire pulse trains, a provision for switching out a single pulse from the mode-locked train has been incorporated. A high-speed electro-optical shutter is used, consisting of two crossed thin-film polarizer pairs (TFP) on either side of a high-speed Lasermetrics 1071-FV Pockels cell, which is switched by a  $\sim$ 7-kV pulse provided by a Lasermetrics type 8601 avalanche-transistor Krytron-triggered Blumlein pulser. The Pockels cell is connected to a  $50\Omega$  terminator via a 30.5-m (100-ft) length of RG-8/U coaxial cable. The thin-film polarizers are at Brewster's angle ( $56.5^\circ$ ) and are stacked in pairs to yield a polarization ratio of  $\sim 2.8 \times 10^{-5}$  for each pair. The output of the laser is horizontally polarized. For convenience the polarization vector is rotated into the vertical plane by a half-wave retarder plate ( $\lambda/2$ ). The first thin-film polarizer rejects any residual horizontal polarization component. After passing through the inactive Pockels cell, the first pulse in the train is totally reflected by the second polarizer stack to an ITT FW 4014 biplanar vacuum photodiode, whose output is displayed on a Tektronix type 519 oscilloscope.

The first laser pulse triggers the oscilloscope. Approximately 45 nsec later a fast-rising step-function voltage pulse appears at the "+ Gate" output of the oscilloscope. This signal is used to trigger the high-voltage pulser which activates the Pockels cell. The + Gate output delay can be continuously varied from 45 to 80 nsec, thus permitting precise timing of the pulse delivered to the Pockels cell. The pulser itself has an additional variable-delay control, which can be set for pulse delays of  $\sim$ 100-400 nsec relative to the triggering signal if desired. The direct mode, which affords a shorter delay of  $\sim$ 35 nsec, has been used in our experiments. The laser pulse that happens to pass through the Pockels cell while it is switched on has its polarization rotated into the horizontal plane and thus passes through the second polarizer unimpeded. The remaining pulses in the train arrive in the Pockels cell after the switching pulse and hence are totally reflected by the second polarizer.

We have been able to switch out clean single pulses with up to 90% efficiency, with a good degree of reproducibility. Generally, about 3 out of 5 shots are successful (i.e.,  $>70\%$  throughput, with no measurable bleed-through

of adjacent pulses), provided the mode-locked pulse train is devoid of any spurious or satellite pulses which could cause premature triggering.

#### Pulse Chronometer System

Temporal width measurement of the selected ultrashort pulse is carried out by means of a picosecond streak shutter that we have used extensively in past work (34,46,56,57). The selected single pulse generates 2nd harmonic light (530 nm) in a KDP crystal tuned to yield an SHG conversion efficiency of about 1%. The superimposed infrared (IR) and green pulses are separated at the dichroic beamsplitter (DBS) (Fig. A-1). For the macromolecular studies a 50% beamsplitter ( $BS_1$ ) directs half the IR pulse energy to the ultrafast streak shutter. (For the primate experiments all the IR energy is directed into the streak shutter, since the irradiation of the eye is carried out with the 2nd or 4th harmonics). The polarization of this pulse is rotated into the vertical plane by a half-wave retarder ( $\lambda/2$ ). Lenses  $L_1$  and  $L_2$  reduce the beam diameter by a factor of four. The pulse then traverses a quartz cell filled with carbon disulfide ( $CS_2$ ). This cell is located between two high-quality crossed polarizers ( $P_1, P_2$ ), whose polarization axes are inclined at 45° with respect to the polarization of the IR pulse. These three components constitute the ultrafast streak shutter. As it travels through the  $CS_2$ , the IR pulse induces a narrow zone of birefringence in its immediate vicinity (46). To an observer viewing the shutter at right angles to the IR path, the effect is that of a narrow "slit" moving across the line of sight at the speed of light in  $CS_2$  ( $1.84 \times 10^{10}$  cm/sec). The shutter thus produces a streak record of light pulses incident at right angles to the IR path.

The 530-nm pulse split off at the dichroic beamsplitter is directed toward the shutter by a right-angle prism (PR) and expanded horizontally by a pair of cylindrical lenses ( $L_3, L_4$ ) to illuminate the entire length of the shutter, where it is sampled by the IR gating pulse. In the case of the primate experiments, only a portion of the 530-nm light is directed to the shutter, by means of a pellicle beamsplitter. The signal exiting from the shutter is a cross-correlation between the gating and green pulses (57). If the depth of the IR gating pulse is small, the transverse dimension of the transmitted green pulse is essentially the same as the geometrical pulse length of the IR pulse in air.

The pulses gated by the shutter are detected and processed by the video detection and display system (VDDS) shown in Figure A-2 (46,57). The shutter output is imaged by a Telemation TMC-1100 CCTV camera equipped with an RCA 4532A silicon vidicon tube. The video signal is processed by the video display control unit (VDC, built in-house) and displayed on an RCA CCTV monitor. Superimposed on the display is a bright rectangular frame generated by the VDC. The frame height can be varied from 1 to 64 TV lines, and its width from an equivalent of 64 lines to full screen width. The intensity profiles of the TV lines within the frame are displayed on an oscilloscope. The VDDS is operated in the single-shot mode, wherein only a single sweep of the vidicon and display oscilloscope occurs. In this case only half the field of TV lines is swept; i.e., only the odd- or even-numbered lines. This avoids charge leakage from the transient image on the vidicon in the time between sweeps of the odd and even fields. Thus, in this mode up to 32 alternate lines can be examined. A trigger output pulse from the VDC fires the laser at the start of the vidicon sweep.

In our studies we have used a frame height of one line and positioned it to provide a horizontal slice through the center of the cross-correlation pulse image. The oscilloscope display is thus a plot of pulse intensity as a function of line. All pulse durations quoted are measured full width at half-maximum and are deconvoluted for the effect of the finite thickness of the birefringent zone in the shutter medium.

#### Pulse Energy Measurement

The IR laser pulse energy is monitored by a Laser Precision RkP-331 pyroelectric energy probe and RkP-3230 digital display unit. This system was calibrated by the manufacturer using standards traceable to the National Bureau of Standards. A 20-cm-f.l. lens placed 10 cm in front of the probe focuses the incident IR pulse to <3-mm diameter for acceptance by the probe aperture. The incident pulse is sampled by means of an uncoated glass beam-splitter (BS<sub>2</sub> in Fig. A-1).

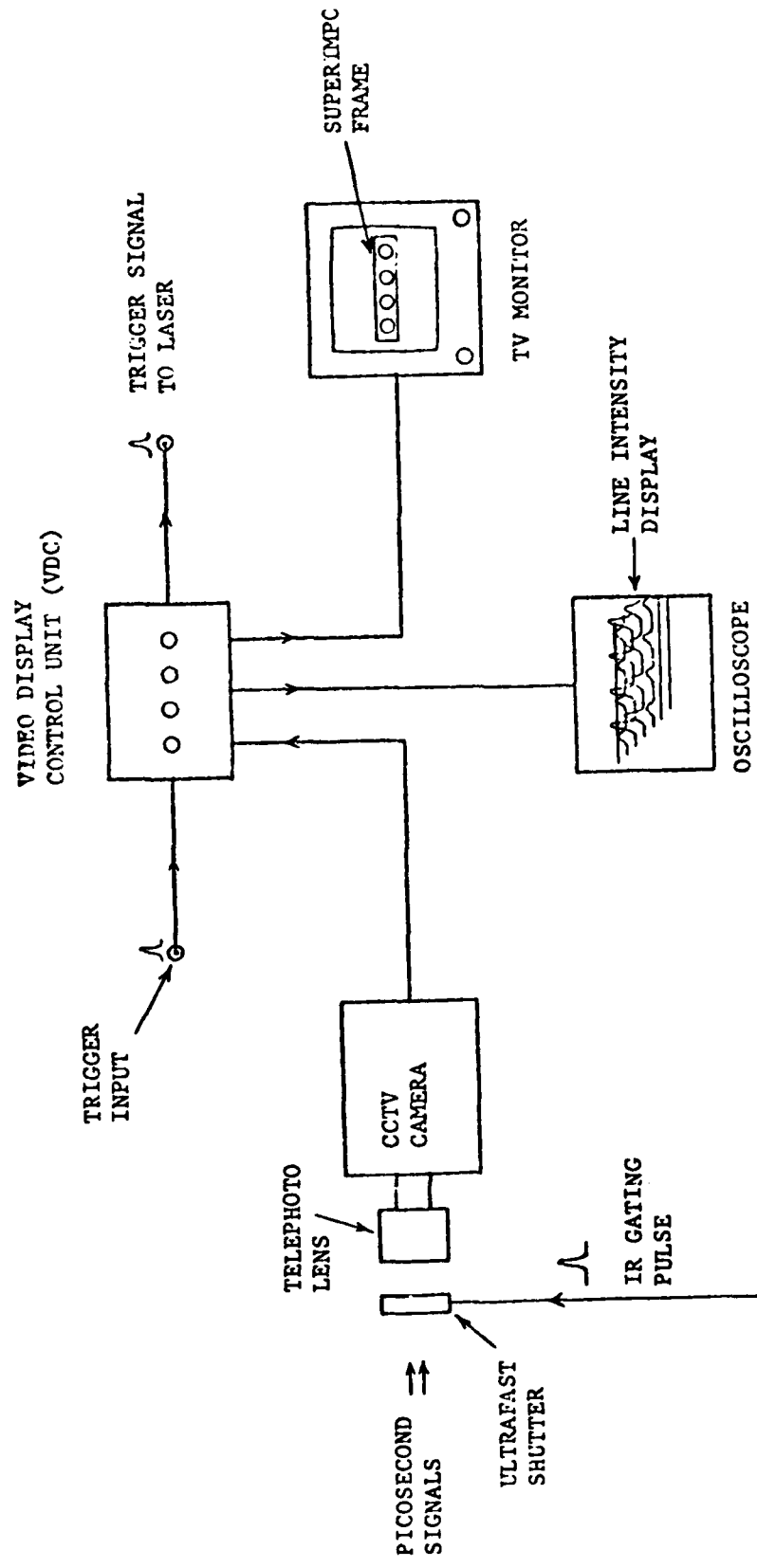


Figure A-2. Schematic of video detection and display system.

## APPENDIX B

### EXPERIMENTAL PROTOCOL FOR DNA STUDIES

Calf-thymus DNA solutions were carefully prepared at a 1-mg/ml concentration in aqueous sodium chloride (NaCl) by dissolving the DNA in a cold room (5°C) for periods of 3-5 days, at a carefully controlled stirring rate of <1 cycle/sec. Some samples included the Ca<sup>++</sup> sequestering agent, EDTA; others did not. In each case both the test and control samples were treated identically except for irradiation by the Nd:Glass laser. Part of the sample solution was used to fill the selected test cell for irradiation by the picosecond laser pulses. An identical cell was filled at the same time to act as the control sample. The test cell was filled carefully to minimize the occurrence of air bubbles at the optical windows or in the optical path of the laser pulse.

Two types of UV-grade fused-quartz test cells were manufactured by Precision Cells, Inc. for the irradiation experiments. One cell type has a 5-mm ID and a 2-cm path length. Two filler spouts at either end are provided for filling and flushing the cell. It is referred to as the "short" cell. The other type is similar in construction to the short cell but has a 2-mm ID and a 10-cm length and is referred to as the "long" cell. It is used when higher incident energy levels are produced by focussing down the incident beam diameter. In each case the incident laser pulse just fills the bore of the cell and thus irradiates the entire sample.

Test samples were irradiated by single mode-locked pulses, entire pulse trains, and successions of several pulse trains. To achieve higher energy densities, the small-diameter long cell was used. The test and control samples were then taken out of their respective cells and diluted with 1-M NaCl solution in the ratio of 0.5 ml DNA to 9.5 ml NaCl. The solutions were filtered through either a 3.0- or 1.25- $\mu\text{m}$  filter and collected in scattering cells for the dynamic light scattering experiments. Sample handling for the gel electrophoresis and low-shear viscometry is discussed in the main text.

## APPENDIX C

### DYNAMIC LIGHT SCATTERING FACILITY

The dynamic light scattering apparatus consists of a CW He-Ne laser operating at 632.8 nm with approximately 50-mW power, the optical detection system, photon counting and correlating electronics, and a PDP-12 computer for data analysis and storage. The block diagram of the experimental setup is shown in Figure C-1. The laser and optical detection systems are mounted on a vibrationally damped table which consists of a 1360-kg, 3.7-m-long, 83-cm-wide-flange, steel I-beam sitting upon 16 free-floating springs grouped into four groups of four. The resonance frequency of the beam with respect to the floor is between 1 and 2 Hz, as per design.

The output of the laser is passed through an optical polarizer and a 10-cm-f.l. lens to focus the laser to its minimum waist in the scattering cell. The optical detection system consists of a low-noise-selected ITT-FW 130 photomultiplier tube with a mu-metal shield enclosed in a specially constructed aluminum housing that contains the photomultiplier dynode bias electronics. The optical detection system is mounted on a triangular optical rail rigidly attached to a rotary milling table.

A portion of the scattered light from the sample passes through a 10-cm lens placed such that the light passing through the lens forms a divergent cone. This is easily achieved by placing the lens so that the distance between the focused laser-beam waist in the sample and the lens is less than the focal length of the lens. A series of apertures between the photomultiplier and the lens admit light from only a rather small solid angle. The actual collection solid angle is ultimately determined by the dimension (0.25 mm) of the photoactive cathode and the divergence angle of the beam, and is slightly less than the coherence solid angle. (Collecting a greater solid angle simply includes more independently fluctuating K-vectors, reducing the apparent signal-to-noise ratio.)

The photomultiplier output is fed to the PAR amplifier-discriminator, which selects the photoelectron pulses and transfers them to the pulse inverter. This in turn converts them to TTL pulses suitable for input to the

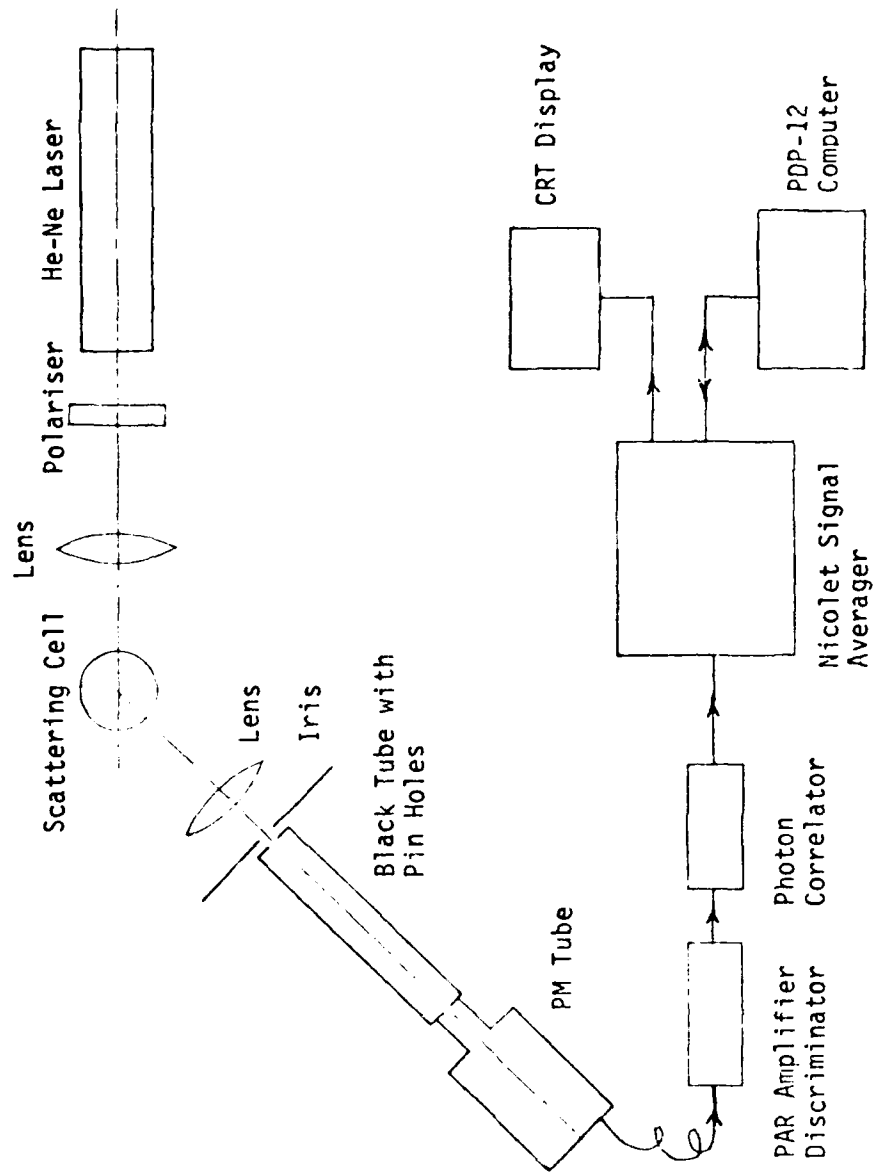


Figure C-1. Experimental arrangement for dynamic light scattering.

digital photon-correlator. The output correlation function is stored in the memory channels of the Nicolet signal averager, which can be transferred to the PDP-12 computer via its A-D converter.

The digital photon-correlator is a 256-channel Chen-type digital clipped correlator (DCC) (58) constructed in-house. A block diagram of the DCC is shown in Figure C-2.

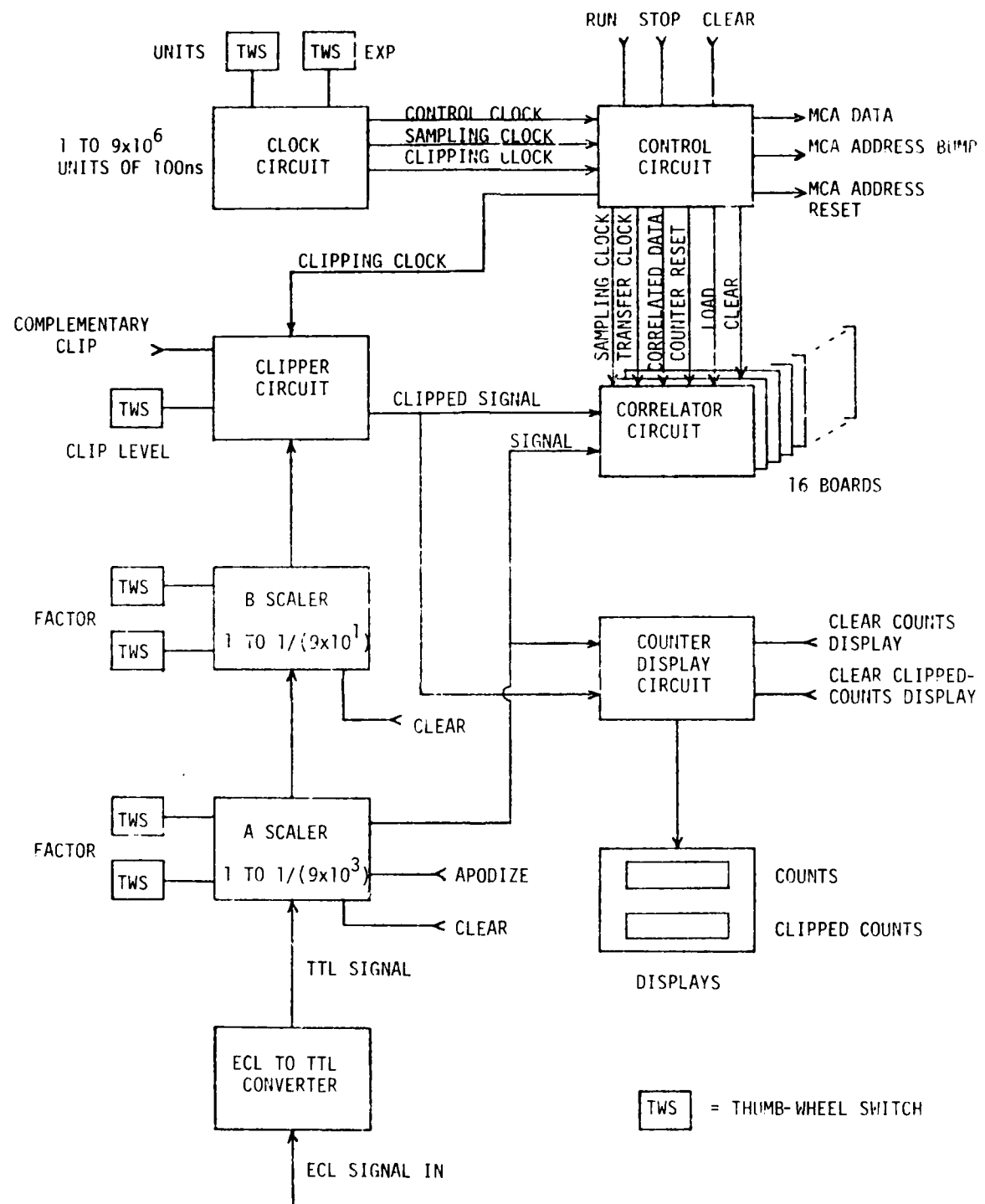


Figure C-2. Block diagram of digital clipped correlator.